Die approbierte Originalversion dieser Diplom-/Masterarbeit ist an der Hauptbibliothek der Technischen Universität Wien (5. OG) aufgestellt und zugänglich (http://www.ub.tuwien.ac.at).

The approved original version of this diploma or master thesis is available at the main library of the Vienna University of Technology (5th floor) on the open access shelves (http://www.ub.tuwien.ac.at/englweb/).

D I P L O M A R B E I T

Results and further Developments of the Qualification Procedures for the CMS Tracker Silicon Microstrip Sensors

ausgeführt am
Atominstitut
der Österreichischen Universitäten

unter Anleitung von
Univ.Doz. Dipl.-Ing. Dr.techn. Manfred KRAMMER

durch
Edmund WIDL
Badgasse 1-7/7/12
1090 Wien

Preface

This diploma thesis has been carried out within the framework of the CMS Tracker Collaboration at the Institute for High Energy Physics of the Austrian Academy of Sciences. Since the goals of the CMS experiment are very ambitious the associated effort to ensure full functionality is accordingly great. Especially for the CMS Tracker project, where an amount of approximately 15000 modules have to be operable within the next few years, appropriate procedures had to be introduced to ensure the needed quality. The aim of my work presented here was to put these procedures, that were often based on experience, on an empirical basis by correlating the experimental results of the sensor qualification with the perfomance of the first assembled modules.
The CMS experiment is highly complex and the collaboration that is working on it is very large. Therefore the first four chapters are thought to be an introduction in order to clearify the relevance and importance of my studies: In chapter 1 I give a short overview of the discovery potential for the four experiments at the LHC currently under construction. The concept of the CMS experiment for detecing this new physics and a brief description of its subsystems is subject of chapter 2. The central full silicon microstrip tracker is described in chapter 3, where a more detailed explanation of its functionality, sensor and module design, readout electronics and overall geometry is given. The implemented qualification and module assembly procedures as well as the Tracker DataBase, that provides all collaboration members access to the corresponding results, are explained in chapter 4. Here I also present the visualDB-application I have developed, a very flexible tool for extracting, processing and histograming data from the database in an appropriate manner. Thus it is a useful tool for monitoring the quality of the sensor production, where problems can show up in a large variety of parameters.
Chapter 5 deals with the topic of depletion voltages, one of the most characteristic parameter for silicon microstrip sensors. To be still operable after an exposure of 10 years to the radiation of the LHC environment, it is important to have sensors with depletion voltages within a certain range. In order to prove that one of the suppliers was using material with bad specifications I developed a theoretical correlation between the depletion voltage of a sensor and a planar diode. The latter is measured on well defined testsructures during production quality control. To get realistic results I also considered the radial distribution of the resistivity on the wafers from which the sensors are produced. By showing that the algorithm, for extracting the depletion voltage from a sensor's CV-curve, is independent over a large range from the frequency of the used LCR-meter probing signal, I also outruled a possible source for a systematic error. To do so, I performed the necessary measurements using the institute's quality control setup. Finally the sensor pairing scheme, based on the values of the corresponding depletion voltages, for modules containing two sensors is introduced.
Chapter 6 concentrates on the IV-behaviour of sensors from the second sensor supplier. After the assembly of the first modules an unexpectedly high failure rate has been observed. Some modules exhibited such an extreme noise on a few chan-

nels, that the performance of whole readout chips was degraded. For this reason I developed a grading scheme with three categories, that emphasized on abnormal IV-curve properties, especially kinks. By assembling only modules of the same grade, a clear improvement could be accomplished. Modules containing sensors of the best category showed a failure rate of less than 5%, whereas modules made of sensors of the least qualitative category showed a failure rate of 15%. To enable the collaboration to perform this grading I developed an application that extracts the necessary information from the database, performs the grading and supplies additional data that is important for module assembly.

The noise performance of the so far assembled modules is subject of chapter 7. By applying concepts of noise theory on a structure like a microstrip sensor, I could prove that the above mentioned problems in the module production are not caused by ordinary leaky strips, i.e. strips exhibiting high leakage currents, as previously assumed. For this reason I firstly examined experimentally that the theoretical noise figure is in agreement with the measurements. Secondly, I correlated the results from single strip scans with noise measurements from assembled modules. I could show that even leakage currents as high as 1 μA increase the noise level 20% at the most. This suggests that other effects, such as the discussed effect of microdischarges, and not usual noise sources are responsible for the high module failure rate. Finally I show a study of the signal-to-noise ratio of assembled modules from last year's testbeam at CERN at which I participated. To process this testbeam data I used a preliminary implementation of the foreseen CMS reconstruction software.

Contents

1 Introduction **6**
1.1 The Large Hadron Collider 6
1.2 Physics at the LHC 8

2 The CMS Experiment **11**
2.1 CMS Detector Layout 11
2.2 The Magnet System 12
2.3 Particle Tracking 13
2.4 Calorimetry 15
2.5 Muon Detection 17

3 The CMS Silicon Microstrip Tracker **20**
3.1 Energy Loss and Charge Collection 20
3.2 Radiation Damages 22
3.2.1 Doping Concentration 22
3.2.2 Leakage Current 22
3.2.3 Charge Collection Efficency 23
3.3 Sensor Design and Specifications 23
3.3.1 General Design 23
3.3.2 Specifications regarding the LHC Environment 25
3.4 Readout Electronics 26
3.5 Tracker Geometry 27

4 Qualification Procedures **31**
4.1 The Quality Assurence Scheme 31
4.2 Sensor Quality Control 31
4.2.1 Optical Inspection 31
4.2.2 Electrical Characterization 32
4.3 Process Control 34
4.4 Module Assembly 36
4.5 The CMS Tracker Database 38
4.5.1 The visualDB-application 38

5 Teststructure and Sensor Depletion Voltages **41**
5.1 Motivation 41
5.2 Theory 43

5.2.1 Basic Equations . . . 43
5.2.2 Potential of a Charged Bulk next to a Conductor . . . 43
5.2.3 Potential of a Charged Plane next to a Conductor . . . 44
5.2.4 Potential of one Charged Strip . . . 44
5.2.5 Depletion Voltage of a Planar Diode . . . 45
5.2.6 Depletion Voltage of a Microstrip Sensor . . . 46
5.2.7 Comparison between Sensor and Diode Depletion Voltages . 48
5.3 Results . . . 48
5.3.1 Correlation for HPK-Sensors . . . 49
5.3.2 Correlation for STM-Sensors . . . 50
5.3.3 Conclusion . . . 51
5.4 Sensor Pairing . . . 54

6 Advanced Sensor Grading 56
6.1 Motivation . . . 56
6.2 The Grading Procedure . . . 58
6.3 Implementation . . . 61
6.4 Results . . . 63
6.4.1 Grading Statistics . . . 63
6.4.2 Failure Rate of Assembled Modules . . . 63
6.5 Conclusion . . . 64

7 Module Noise Performance 65
7.1 Motivation . . . 65
7.2 Noise Performance . . . 65
7.2.1 Theory . . . 65
7.2.2 Common Mode and Pedestal Subtraction . . . 67
7.2.3 Results . . . 68
7.3 Signal-to-Noise Ratio . . . 75

8 Conclusions 77

Chapter 1

Introduction

1.1 The Large Hadron Collider

In order to push todays limits in high energy physics and to further investigate the Standard Model and its extensions CERN decided to dismantle the Large Electron Positron Collider (LEP) in 2001 and started the construction of the Large Hadron Collider (LHC) in the existing 27-kilometer LEP tunnel. The LHC is planned to be operable in 2007 and run for at least 10 years.
The principal idea of colliding machines, like LEP or LHC, is to have two independend particle beams, divided in small bunches, which are accelerated in oposite direction along more or less circular-shaped trajectories. These trajectories are crossing at well defined points, the so called collision points. Around these collision points detectors are built in order to measure the interacions of the colliding particles.
The advantage of such colliding beam experiments lies in the fact, that they are resting in the center-of-mass system of the interacting particles and can therefore

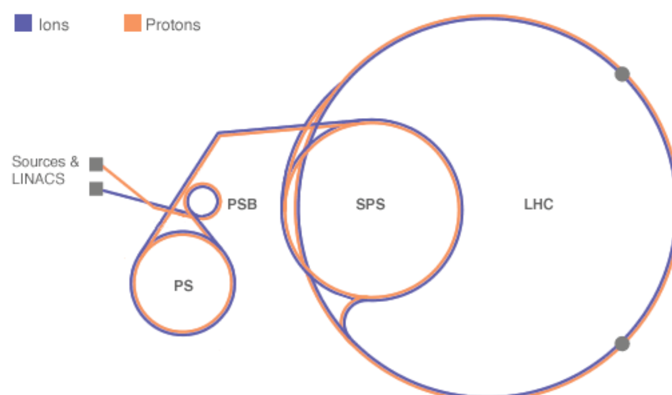

Figure 1.1: Sketch of the CERN accelerator complex showing the particle sources for protons and ions, the LINACs (Linear Accelerators), the PSB (Proton Synchrotron Booster), the PS (Proton Synchrotron) and the SPS (Super Proton Synchrotron) which are finaly loading the LHC.

use the particles' whole energy for the physics studies. So called fixed target experiments can in contrast only use a fraction of the incident particle's energy that scales with its square root and also depends on the interacting particles' masses. Colliders are primarily discribed by two parameters:

- The *beam energy* E_{beam} determines the center-of-mass energy E_{cms} at the collision point which can in principle be fully used to create new particles. For particles, that have a substructure, such as nuclei or hadrons, of course only the center-of-mass energy of the actual colliding constituents is relevant. As mentioned above, for colliding beam experiments E_{cms} is simply two times the beam energy, since the center-of-mass is not moving with respect to the collision point.

- The *luminosity* $\mathcal{L}$ describes the possibility of an interaction between the particles of two colliding bunches. This means that for a given process with an interaction cross-section σ the event rate R can be calculated via:

  $$R = \mathcal{L}\sigma \tag{1.1}$$

  The luminosity at a given bunch-crossing frequency f, with bunches containing n particles is then given by:

  $$\mathcal{L} = f\frac{n^2}{4\pi\sigma_{\mathrm{x}}\sigma_{\mathrm{y}}} \tag{1.2}$$

  The parameters σ_{x} and σ_{y} in above equation characterize thereby the beam spread in horizontal and vertical direction.

Although the concept of colliding beams and repetitve acceleration is superior in comparrison to most other methods, it has one drawback: When charged particles become accelerated along a circle-shaped trajectory with a radius R, they start to radiate so called *synchrotron radiation* which leads to an energy-loss (for highly relativistic particles with $E \simeq pc$ and a cycle duration T):

$$\frac{\mathrm{d}E}{\mathrm{d}T} = \frac{e^2 c}{6\pi\epsilon_0 R^2}\frac{E^2}{(m_0 c^2)^4} \tag{1.3}$$

Problems arise when at a certain velocity the energy loss per turn is equal to the input energy which makes a further acceleration impossible. In order to prevent that, one has two possibilties: Increasing the colliders's diameter or accelerating heavier patricles.
This finally lead to the decission to install a proton-proton collider instead of LEP, since protons are 1836 times heavier than electrons or positrons respectively, even if proton-proton interactions are due to the proton's quark composition not as easy to predict as electron-positron interactions. The LHC will be able to accelerate protons up to 7 TeV with a maximum luminosity of $\sim 10^{34}\mathrm{cm}^{-2}\mathrm{s}^{-1}$ and a bunch crossing every 25 ns and, in addition, heavy ions up to 1250 TeV with a luminosity of $\sim 10^{27}\mathrm{cm}^{-2}\mathrm{s}^{-1}$ and bunch crossings every 125 ns.

1.2 Physics at the LHC

During the last decades a theory of elementary particles and their interactions, the so called Standard Model of Elementary Particles (SM), has been developed. This model was extensively tested and the predictions were allways in amazing agreement with the experimental results.
In this model one can distinguish between two kinds of particles (see also table 1.1):

- Spin-1 bosons: These bosons, also called gauge bosons, are carrying the three fundamental forces that are described in SM, namely the electromagnetic, the weak and the strong force.
- Spin-1/2 fermions: These fermions form the observable matter in the universe.

The SM provides a very elegant theoretical framework where the existance of force-carrying gauge bosons comes up automatically from some fundamental symmetries ($SU(3)_C \otimes SU(2)_L \otimes U(1)_Y$). Furthermore the electromagnetic and the weak interaction are naturally unified in the so called *electroweak interaction*, similarly as magnetic and electrostatic phenomena are unified in the Maxwell-theory.
Nevertheless it has one drawback: All gauge bosons are massless within this concept unless one introduces a spin-0 field, called the *Higgs-field* ϕ, which itself is not satisfying these symmetries because of a non vanishing vacuum expectation value $\langle\phi\rangle$. This is referred to as *electroweak symmetry breaking*. From interactions with this field the $W^{\pm}$- and Z^0-bosons acquire masses proportional to $\langle\phi\rangle$, while the photon remains automatically massless. In addition, this mechanism can also be used within this framwork to give masses to the massive leptons and the quarks.
The existance of such a Higgs-field implies in quantum field theory also the existance of excited states – or with other words: the existence of Higgs-particles. Unfortunately, the Higgs-particle is the only particle predicted by the SM that has not been detected yet, most likely due to its huge mass.
Furthermore the SM is known to be incomplete. Topics like for instance the neutrino's mass or the unification of elctroweak and strong interaction are not contained. Therefore new theories, like the Minimal Supersymmetric Standard Model, have been developed that extend the SM and which predict a lots of yet still unobserved new physics.
The main goal of the LHC-experiments within this concept can be summarized as follows:

- Investigate the mechanism of elektroweak symmetry breaking by identifying Higgs-events in order to approve the predictions of the SM or one of its possible extensions. For the latter it will be also of great importance to look for other predicted effects like for example the existance of supersymmetric particles. The ATLAS and CMS experiments were primarily designed to attain this goals.

In addition, two other important issues will be addressed for a further investigation of the SM and its limits:

Spin-1/2 fermions: constituents of matter

leptons		mass [GeV/c^2]	charge [e]	quarks		mass [GeV/c^2]	charge [e]
electron neutrino	ν_e	$< 1\times10^{-8}$	0	up	u	0.003	2/3
electron	e	0.000511	-1	down	d	0.006	-1/3
muon neutrino	ν_μ	< 0.0002	0	charm	c	1.3	2/3
muon	μ	0.106	-1	strange	s	0.1	-1/3
tau neutrino	ν_τ	< 0.02	0	top	t	175	2/3
tau	τ	1.7771	-1	bottom	b	4.3	-1/3

Spin-1 bosons: force carriers

name	mass [GeV/c^2]	charge [e]	force
photon γ	0	0	electromagnetic
W^-	80.4	-1	weak
W^+	80.4	+1	
Z^0	91.187	0	
gluon g	0	0	strong

Table 1.1: Particles of the Standard Model

- CP-violation: The violation of the CP-symmetry, i.e. the symmetries between particles and antiparticles as well as parity, is maybe the key to understand why there exists almost only matter and no antimatter in the observable universe. The LHCb experiment will mainly focus on this topic.
- Heavy Ion Physics: By colliding heavy nuclei it is possible to create for a short time conditions like within the first microsecond after the big bang. This special phase of matter, called *quark-gluon-plasma*, will be researched mainly by the ALICE experiment.

For this physics program the LHC will be a powerfull tool since it will provide the needed energies at a luminosity that allows to take the data within a reasonable time. For an example see figures 1.2 and 1.3 that show a summary of the SM Higgs-physics, i.e. the dominant decay-channels as a function of mass that allow to cover the complete mass range, and the therefore needed luminosities respectively.

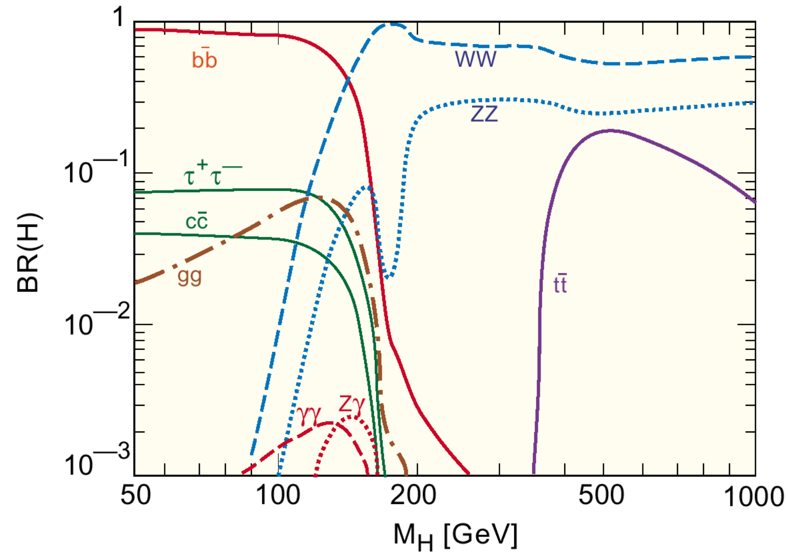

Figure 1.2: Branching ratios for the SM Higgs-boson as a function of its mass.

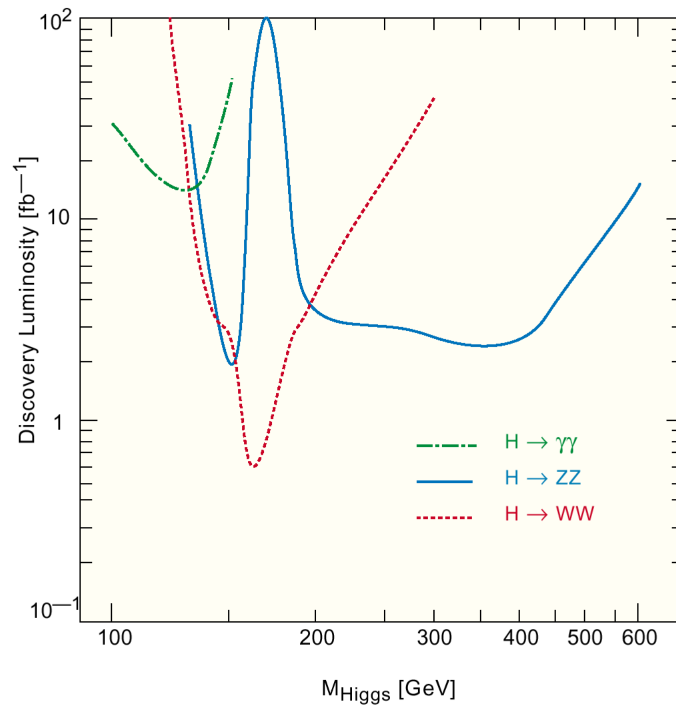

Figure 1.3: Luminosity required for SM Higgs discovery within one year, i.e. $5\,\sigma$ signal-to-background ratio, as a function of the mass of the Higgs-boson.

Chapter 2

The CMS Experiment

2.1 CMS Detector Layout

The Compact Muon Solenoid (CMS) is one of four experiments for the Large Hadron Collider apparently under preparation [1]. It was designed as multi-purpose experiment even if the overall design was optimized to especially discover new physics underlying the elctroweak symmetry breaking. Though several theoretical possibilities exist the Higgs-mechanism in the context of Supersymmetry is the favoured one. Of course also the search for SM Higgs-bosons was emphasized such that the whole expected mass range from $80\,\mathrm{Gev} < \mathrm{M_H} < 1\,\mathrm{TeV}$ will be covered by the experiment. Many experimental signatures from this new physics are possible involving high transverse energy muons, electrons, photons and jets. In order to cleanly detect these signatures the identification and precise measurement of

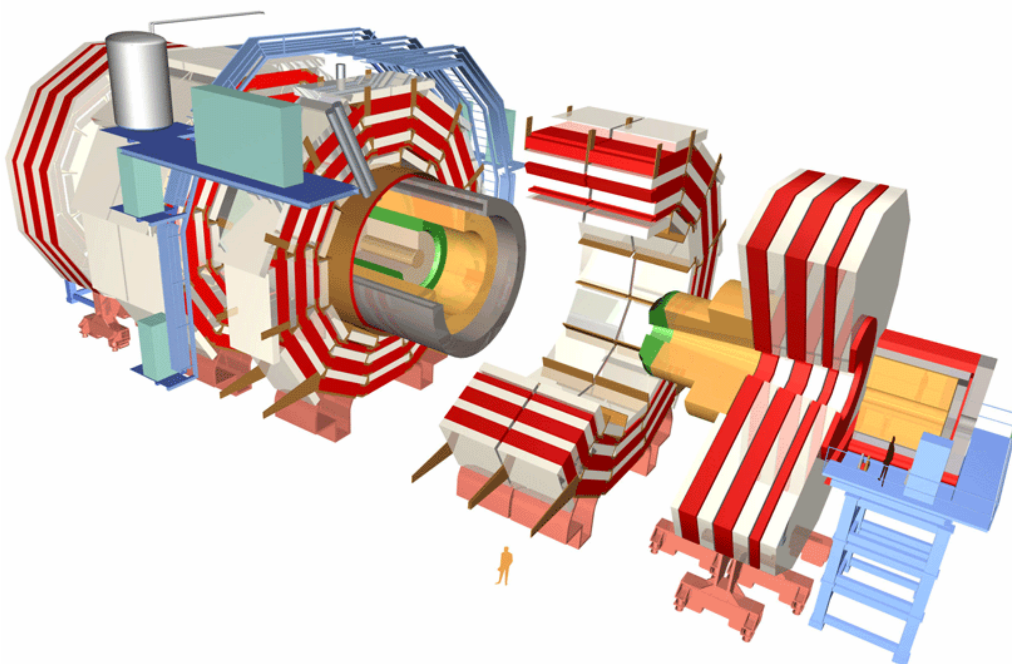

Figure 2.1: Drawing of the CMS Detector

muons, electrons, photons and jets over a large energy range and at high luminosity is essential.
Besides the Higgs-search at high luminosity the detector was also well adapted for the initial low luminosity phase of LHC where studies about CP-violation or quark-gluon-plasma can be done.

For this reasons the main design goals of CMS are:

1. A highly performant muon system
2. The best possible electromagnetic calorimeter consistent with 1.
3. A high quality central tracking to achieve 1. and 2.
4. A hadron calorimetry with sufficient energy resolution and good hermiticity.

Therefore the detector, 15 m in diameter, 21.6 m long and with a weight of 12500 t, will consist of a 4 Tesla superconducting solenoid surrounded by a massive iron return yoke with inserted muon chambers. The tracking system together with the electromagnetic and the almost hermetic hadronic calorimeter will be placed inside the solenoid. The four subdetector-systems will be arranged in concentric cylinders arround the beamline (barrel region) or in disks perpendicular to the beamline (endcaps).

2.2 The Magnet System

The choice of a 4 Tesla solenoidal field for the CMS detector was made for mainly three reasons [2]:

- The field of a solenoid is in contrast to a toroid parallel to the beamaxis. Thus the bending of the tracks of charged particles is in the transverse plane. In this plane the small beamspread determines the transverse position of vertices to an accuracy of about 20 μm and therfore facilitates the selection of events based on tracks pointing back to the vertex.
- Higher fields increase the momentum resolution and hence the mass reolution of decayed particles. For example:

State	mass resolution at 4T	mass resolution at 3T
$H_{SUSY}(300\,GeV) \rightarrow ZZ \rightarrow 4\mu$	2.1 GeV	2.8 GeV
$H_{SM}(150\,GeV) \rightarrow ZZ^* \rightarrow 4\mu$	0.8 GeV	1.1 GeV
$Y \rightarrow \mu\mu$	36 MeV	48 MeV

- Interesting events will mainly include particles with high transverse momenta being detected in the outer regions of the detector. The part of the background that consists of charged particles with low transverse momenta can be kept within the inner regions due to the stronger bending by the magnetic field.

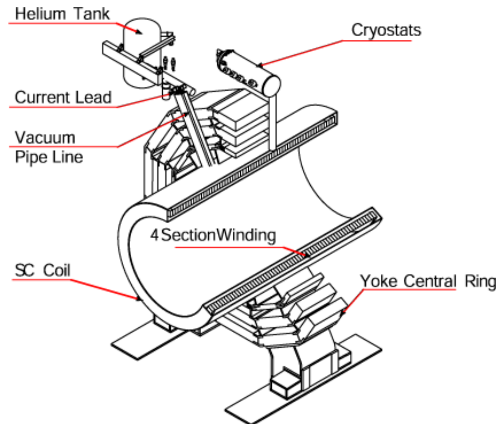

Figure 2.2: Open view of the superconducting coil inside its vacuum tank.

The superconducting coil system itself consists of the coil and the ancillary subsystems required for its operation. The substructure of the superconducting coil is self-supporting, whereby magnetic forces are resisted where they are produced. As the forces induced in the conductor by the magnetic and thermal loads go beyond the yield stress of pure aluminium a metallurgically bonded mechanical reinforcement structure is surrounding the four layer coil.
The external cryogenic sub-system consists of the compressors, the cold box, the vessels containing 200 m^3 pressurized He-gas, the 5000 litre liquid He container and the cryogenic line. The cold box and the container for the liquid He will be installed near the magnets while the compressors and the pressure vessel will be at the surface.

2.3 Particle Tracking

As mentioned above, for the CMS experiment events including particles with high transverse momenta are of great importance. Quantifying a particles momentum from its track within a magnetic field is one of the tasks of a Tracker. The principal idea comes from the fact, that the trajectory of a particle with the electrical charge q inside a magnetic field of strength B, having a transverse momentum p_{T} w.r.t. the magnetic field, is a helix with curvature R. The curvature R is determined via:

$$p_{\mathrm{T}} = qBR \tag{2.1}$$

By equiping the volume around the collision point with several layers of particle detectors having at least an one-dimensional spatial resolution one can reconstruct the (projected) trajectories from the measuring points and calculate the (transverse) momenta.
In addition one can achieve to reconstruct the position of vertices by mounting high granularity detectors close to the collision point. This facilitates to distinguish between primary and secondary vertices which is the second important task of a Tracker. Especially for the identification of particles with very short lifetimes that decay almost immediately after production this is of great importance.

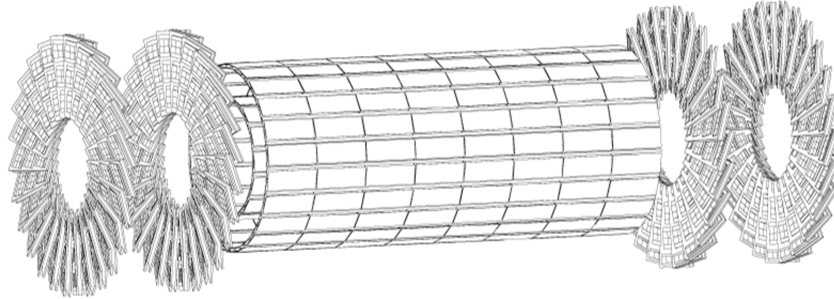

Figure 2.3: High-luminosity configuration of the CMS pixel detector.

distance from beamline	fluence $[n_{eq}\,cm^{-2}]$	technology
> 50 cm	10^{13}	p-type strips on 500 μm thick n-type bulk, high resistivity ($\sim 5K\Omega\,cm$), pitch $\sim 200\mu m$
20 - 50 cm	10^{14}	p-type strips on 320 μm thick n-type bulk, low resistivity ($\sim 2K\Omega\,cm$), pitch $\sim 80\mu m$
< 20 cm	10^{15}	n^+-type pixels on 270 μm thick n-type bulk, low resistivity ($\sim 2K\Omega\,cm$), oxygenated

Table 2.1: Technologies used in the CMS Tracker to match the specifications for radiation hardness and detector occupancy.

In the case of CMS, where thousands of tracks are expexted to cross the inner part of the detector at each bunch crossing, a multi-layer full-silicon Tracker [6] will be installed to meet these requirements. Due to the aggressive LHC environment the use of radiation hard silicon detectors is inevitable if one forsees a lifetime of ten years (see table 2.1). The innermost part, mostly used for vertex reconstruction, will be made of pixel detectors. Several layers of single- and double-sided silicon microstrip detectors will be mounted around the pixel detector in order to be able to track the particles over a large volume with high accuracy. This outer part of the Tracker will be discussed in chapter 3 in more detail.
Silicon pixel detectors are characterised by their two-dimensional spatial resolution and high granularity due to the special geometry. Thus they are very suitable for being used as vertex detectors. For the CMS experiment a pixel system with 2 endcap layers on each side and 3 barrel layers for the low-luminosity phase of LHC is planned. For the the high-luminosity phase only 2 barrel layers are foreseen to be operated (see figure 2.3), because of the radiation damages in the innermost layer. Each barrel will consist of 8 detector modules, which are themselves connected to 16 readout chips. The endcaps consist of turbine disks, each having 24 blades. A blade has 7 detector modules of varying size from 2 to 10 chips.

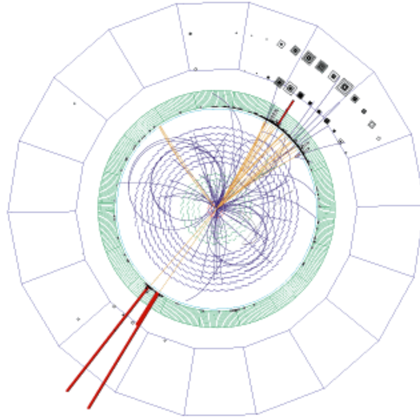

Figure 2.4: Event display for the simulation of a 180 GeV Higgs-bosons decaying into two Z^0-bosons, which in turn decay into an electron-positron pair (seen as red bars in the ECAL) and two hadronic jets (seen as blocks in the HCAL).

2.4 Calorimetry

Calorimetry, i.e. measuring directly a particle's energy, is as well essential for the CMS physics program. Especially the decay-channels of the Higgs-boson into two photons or an electron-positron pair plus two hadronic jets (see figure 2.4) are of great importance if one wants to cover the whole mass range. Also the measurement of the integral energy of all detected particles is essential for detecting neutrinos via missing energy.

The purpose of *electromagnetic calorimeters* (ECALs) is to totaly absorb electrons and photons via electromagnetic interactions that lead to *electromagnetic showers*. Heavier leptons, such as muons, and hadrons are normally not absorbed due to their high mass, which drastically decreases their energy deposit. As the depth of such a shower increases also the number of secondary particles increases, while their mean energy decreases. As the energies fall below the *critical energy* ϵ, the multiplication process ceases and the energy can be dissipated via ionisation and excitation processes.

The fundamental quantity that describes the performance of an ECAL is the so called *radiation length* X_0. Within one radiation length an electron or photon typically undergoes one interaction within the ECAL's crystals; for an electron this means to radiate a photon, while a photon creates an electron-positron pair. Furthermore the *Moliere radius* describes the transverse dimension of such electromagnetic showers. The scintillation light produced from this electromegnetic showers is then a direct measure of the initially incidenting particle's energy.

For the CMS ECAL [5] all terms making up the energy resolution have to be kept small and should be roughly equal at photon enegies corresponding to approximately half the Higgs mass[1]. Therefore it will consist of over 80,000 scintillating lead-tungstate crystals ($PbWO_4$) that meet these requirements (see figure 2.5).

[1]Especially in the range 100 GeV $< M_H <$ 140 GeV where the two photon channel is most important.

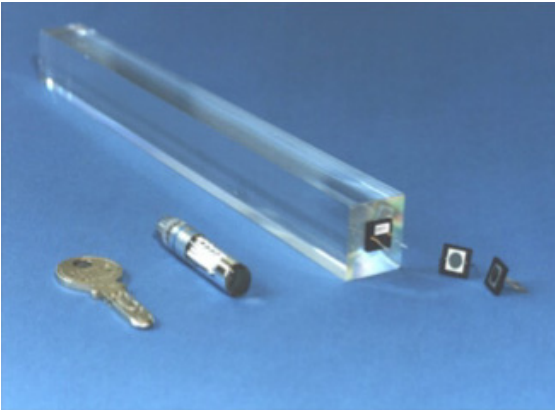

Figure 2.5: Picture of a lead-tungstate crystal ($PbWO_4$) from the barrel of the CMS ECAL.

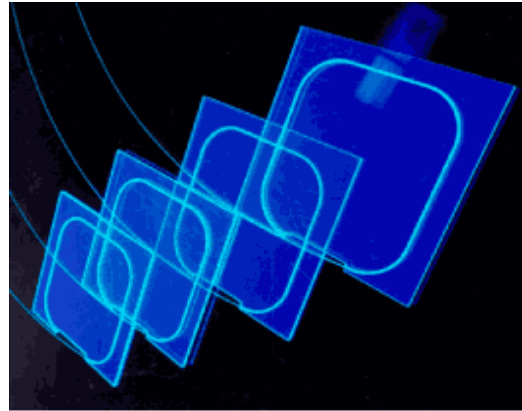

Figure 2.6: Scintillators from the CMS HCAL with inserted wave-length-shifting fibres.

These crystals, that were specially designed for the CMS ECAL, have a short radiation length, a small Moliere radius and are very radiation hard. Radiation affects neither the scintillation mechanism nor the light yield along the crystal but only the transparancy. This light loss will be monitored by a light-injection system an can therefore be measured and compensated. For readout the crystals will be equiped with avalanche photodiodes or vacuum phototriodes and the associated electronics.
In *hadronic calorimeters* (HCALs) hadrons interact via strong interactions with nuclei in dense matter in order to create *hadronic showers*. In principle their functionality is very similar to ECALs. The showers consist of an electromagnetic component, mostly arising from π^0-production, and a hadronic component. Thereby the multiplication process continues until the pion production threshold is reached. In analogy to ECALs the fundamental quantity that describes a HCAL is the so called *radiation length* λ.
HCALs normally consist of a sandwiched structure that are made up alternately of a dense absorber material in which the shower development takes place and detection layers that measure the released energy. For the barrel and the endcaps of the CMS HCAL [3] copper has been chosen as absorber and plastic scintillators for signal detection. The scintillating tiles will use thin wavelength-shifting fibers that guide the signals to the readout (see figure 2.6). Since the barrel HCAL inside the coil is not sufficiently thick to fully contain high energetic showers, additional scintillation layers are placed just outside the coil. The two forward calorimeters, one located at each end of the detector, are situated in a harsh radiation field and can therefore not be constructed of conventional materials. Instead the absorbers are made of steel, which suffers less activation under radiation than copper, and the showers are sampled by radiation resistant quartz fibres.

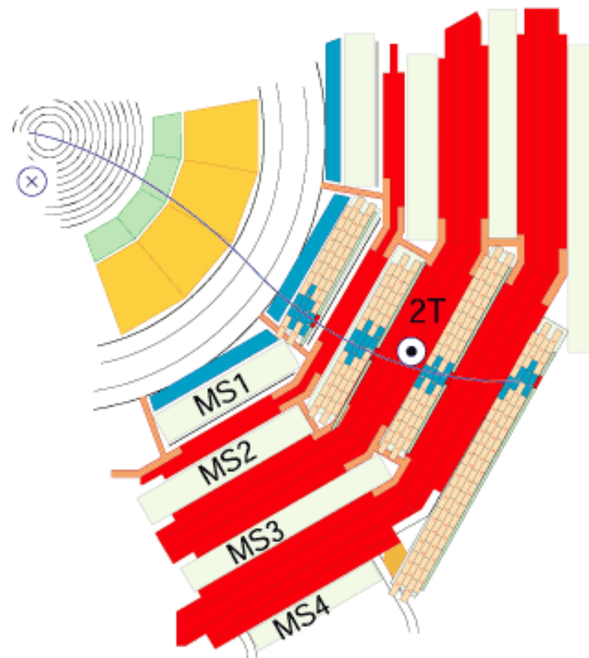

Figure 2.7: Schematic front view of the muon detector barrel.

2.5 Muon Detection

Muons are expected to provide clean signatures for a wide range of physics processes. The task of the muon system [4] is to identify muons and provide, in association with the Tracker, a precise measurement of their momentum. In addition, the system provides fast information for selecting events.
The muon detectors, placed behind the calorimeters and the coil, consist of four muon stations interleaved with the iron return yoke plates. Muon identification is ensured by the large thickness of the absorber material (iron), which can not be transversed by any other particles except neutrinos. There are at least 10 interaction lenghts of calorimeters before the first station and an additional 10 λ of iron before the last station. The identification is achieved by lining up the hits in at least two out of the four muon stations. The presence of multiple stations also enables the identification of faulty hits, coming from hadronic shower punchthroughs and hard muon bremsstrahlung.
All stations consist of gaseous detectors. The principle functionality of these detectors is very simple: They consist of gas-filled volumes in which electrons and ions are produced when an ionising particle traverses it. In order to collect these charges an electric field has to be applied such that the liberated charge carriers are moving to the electrodes. Nevertheless the number of charges produced is normally very small and thus the signal has to be amplified. This is normally done via gas-amplification: If a high electric field is applied in a gas, it causes a free charge to be accelerated until its energy is sufficiently large to ionise other gas-molecules. This process of course continues with the secondary charges as well and thus leads to an avalanche-effect and a measureable signal.
In the barrel, where the magnetic field is guided and almost fully trapped by the

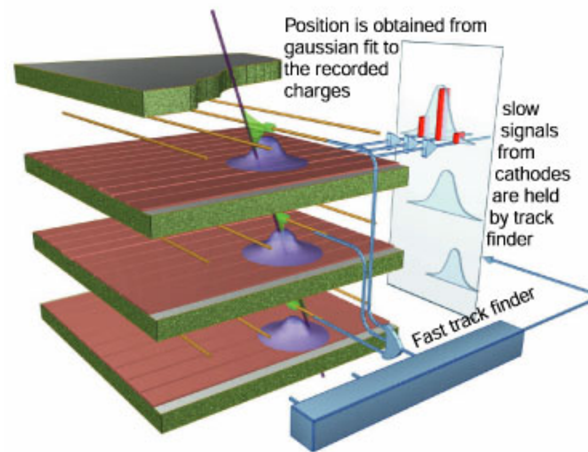

Figure 2.8: Schematic view of a CSC chamber, with a sketch of the mechanism of signal detection.

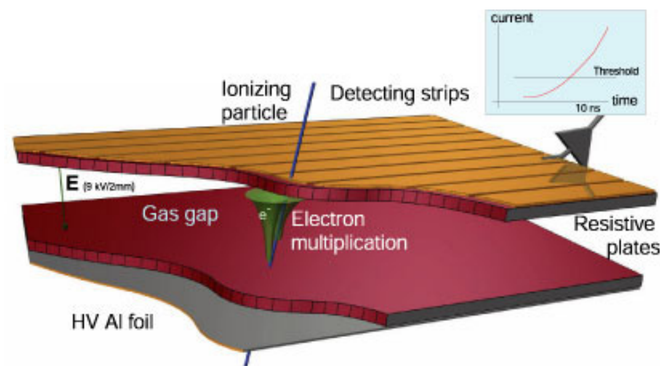

Figure 2.9: Schematic view of a RPC chamber, with a sketch of the signal's time evolution.

iron plates of the magnet yoke, *Drift Tubes* (DT) are used. In DTs the gas-filled chambers are subdivided by conducting plates (equally spaced with a distance of 40 mm) between which thin wires are spanned. The wires are on positive potential w.r.t. the plates such that they attract the produced electrons. The gas-amplification takes place close to the thin wires where the electric field is very high. The coordinate on the plane perpendicular to the wire is obtained from the time taken by the ionisation electrons to migrate to the wire. This time, measured with RPCs with a precision of $\sim$1 ns (see below), multiplied by the electron drift velocity in the gas, translates to the distance from the wire.
In the endcap regions, where the field is very intense (up to several Tesla) and very inhomogenious, *Cathode Strip Chambers* (CSC) are used. CSCs work similar to DTs, but the cathodes are not placed in between the wires but perpendicular below them. This has the effect, that the positive ions, that are produced during gas-amplification, yield in combination with the electrons, that arrive at the wires, a two-dimensional signal (see figure 2.8). In addition to providing precise space and time information, the closely spaced wires make the CSC a fast detector. Every endcap module will contain 6 layers of CSC detectors, whereas the wires give the

radial coordinate and the strips measure ϕ.
Resistive Plate Chambers (RPC) are fast gaseous detectors that allow a precise timing. They combine a good spatial resolution with a time resolution of 1 ns, comparable to that of scintillators. The RPC is a parallel plate counter with the two electrodes made of very high resistivity plastic material. This allows the construction and operation of very large and thin detectors that can operate at a high rate and with a high gas gain without developing streamers or catastrophic sparks. The high gain, due to the gas-amplification in the high electric field, and the thin gap results in a small but very precise delay for the time of passage of an ionising particle. The high resistivity electrodes are transparent to the electric signals generated by the current of the avalanche: the signals are picked up by external strips. The strips are oriented parallel to the DT's wires in the barrel and to the radial strips in the endcap CSCs.

Chapter 3

The CMS Silicon Microstrip Tracker

3.1 Energy Loss and Charge Collection

The fundamental principle of particle detectors is to measure the physical effects caused by interactions between traversing particles and well defined states of matter. A broad variety of different effects can be used, reaching from the production of Cherenkov radiation to nuclear processes. In the case of silicon detectors the energy loss of charged particles due to the excitation of atomic electrons is used. The differential energy loss per mass surface density [$\mathrm{MeV}(\mathrm{g\,cm^{-2}})^{-1}$] was firstly described by H.A. Bethe and F. Bloch [7]:

$$-\frac{1}{\rho}\frac{\mathrm{d}E}{\mathrm{d}x} = C_0 z^2 \frac{Z}{A}\frac{1}{\beta^2}\left[\frac{1}{2}\ln\left(\frac{2m_\mathrm{e}c^2\beta^2\gamma^2T_\mathrm{max}}{I^2}\right) - \beta^2 - \frac{\delta(\gamma)}{2} - \frac{C}{Z}\right] \quad (3.1a)$$

$$C_0 = 4\pi N_\mathrm{A} r_\mathrm{e}^2 m_\mathrm{e} c^2 \quad (3.1b)$$

N_A, Z and A are Avogadro's constant, the atomic number and the atomic mass of the traversed matter, m_e and r_e are the electron mass and its classical radius and ze is the incident particle's charge. T_max is the maximum kinetic energy still detected in the material, I is the mean excitation energy, $\beta = v/c$ and $\gamma = (1-\beta^2)^{-1/2}$. $\delta(\gamma)$ is a correction term due the shielding of the particle's electric field by the electrons. The so called shell correction term C comprises the fact that the assumption of static atoms is not fulfilled for traversing particles with low energy.
For thin layers an additional correction has to be done in equation (3.1a), due to the fact that a fraction of the deposited energy is carried off by so called δ-electrons [8]:

$$-\frac{1}{\rho}\frac{\mathrm{d}E}{\mathrm{d}x} = C_0 z^2 \frac{Z}{A}\frac{1}{\beta^2}\left[\frac{1}{2}\ln\left(\frac{2m_\mathrm{e}c^2\beta^2\gamma^2T_\mathrm{upper}}{I^2}\right) - \beta^2\left(1+\frac{T_\mathrm{upper}}{T_\mathrm{max}}\right) - \frac{\delta(\gamma)}{2} - \frac{C}{Z}\right] \quad (3.2a)$$

$$T_\mathrm{upper} = \inf(T_\mathrm{max}, T_\mathrm{cut}) \quad (3.2b)$$

T_cut in above equation depends on the particle momentum as well as on the material. The number of free charge carriers thereby produced, i.e. electron-hole pairs

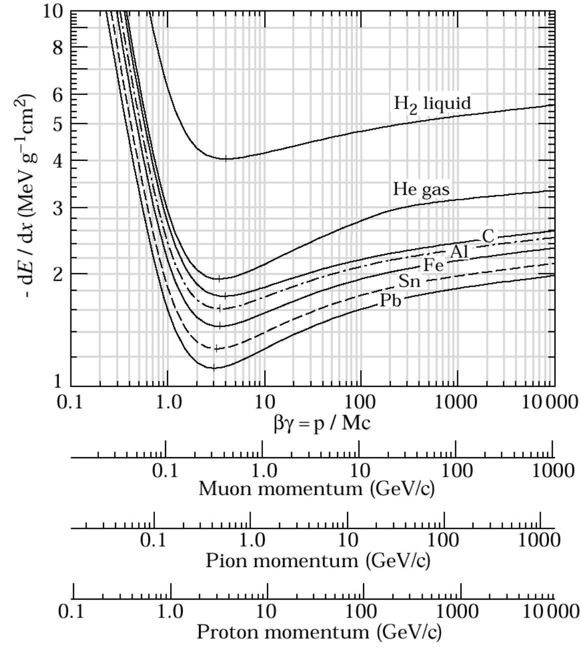

Figure 3.1: Differential energy loss per mass surface density in dependence on $\beta\gamma$ (reduced momentum) for different particles and materials.

in the case of semiconductors, depends on the total energy loss E_{loss} and can be calculated via:

$$n = \frac{E_{\text{loss}}}{E_{\text{eh}}} \tag{3.3a}$$

$$E_{\text{eh}} = 3.6\,\text{eV} \quad \text{(silicon)} \tag{3.3b}$$

Note in above equation, that the average energy to produce an electron-hole pair E_{eh} is not simply the energetic difference between valence band and conductivity band. It also comprises energy losses due to other excitations like phonons or photoeffect.
In order to collect these charges in a semiconducting material a depleted pn-junction is used. This has two big advantages:

- Due to the electric field caused by the junction the charge carriers become seperated and drift to the electrodes. This reduces recombination and is essential to get a measurable signal.
- In case of depletion, when almost no intrinsic charge carriers are present because of the applied reverse bias voltage, the signal-to-noise ratio is reasonable. In undepleted silicon the density of instrinsic charge carriers is of the order $p = n = n_{\text{i}} \approx 10^{10}\,\text{cm}^{-3}$ (thermal equilibrium at about T=300 K) while the signal produced by a MIP[1] traversing 300 μm silicon consists of only ~22000 electron-hole pairs.

[1]MIP = Minimum Ionising Particle. This expression referes to traversing particles that produce a minimum number of charge carriers due to excitation.

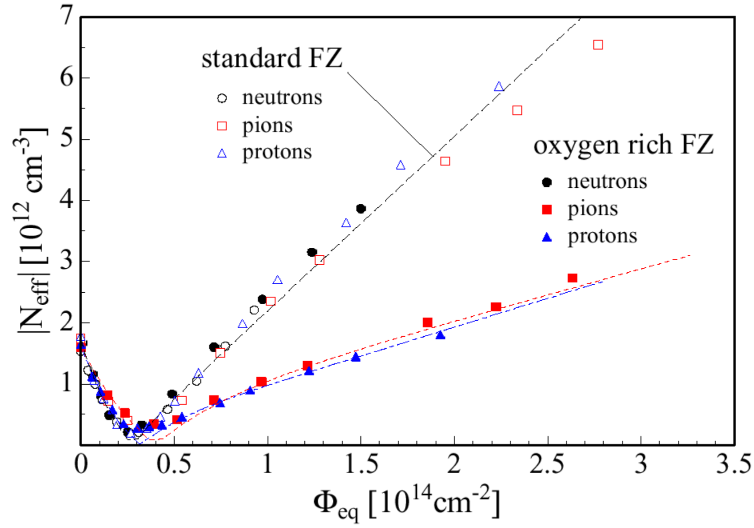

Figure 3.2: Dependence of the effective doping concentration on the 1MeV neutron equivalent fluence for standard and oxygenated silicon [9]. FZ stands for Float Zone and indicates only the production process.

3.2 Radiation Damages

3.2.1 Doping Concentration

Irradiation causes in n-doped semiconductors both the removal of donors and the generation of acceptor-like defects. This effect leads to a change of the effective doping concentration:

$$N_{\mathrm{eff}} = |N_{\mathrm{D}} - N_{\mathrm{A}}| \tag{3.4}$$

N_{D} and N_{A} are the concentrations of donor-like and acceptor-like impurities respectively.

Therfore the effective doping concentration in a n-type semiconductor decreases with the absorbed dose until it behaves as if it was intrinsic. This state is known as the *inversion point*. With further irradiation the acceptors begin to dominate and the previously n-type semiconductor becomes effectively p-type. This effect, called *type inversion*, can be influenced by additional contaminations, like for instance oxygenation (see figure 3.2).

3.2.2 Leakage Current

Radiation damages lead also to an increase of the leakage current I_{leak}, which is strictly proportional to the equivalent fluence Φ_{eff} and the sensitive volume V:

$$\Delta I_{\mathrm{leak}} = \alpha \Phi_{\mathrm{eff}} V \tag{3.5}$$

The so called *current related damage rate* α is independend from material type and resistivity.

After irradiation the increased current is still changing due to a short-term effect called *annealing* with a time constant of a few days at room temperature.

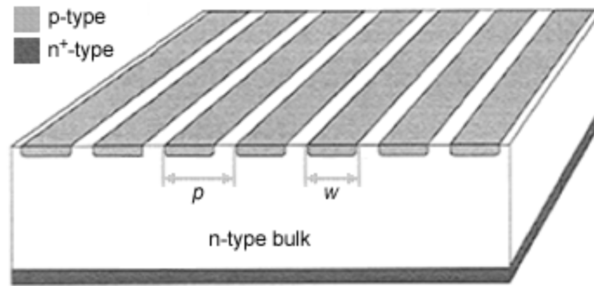

Figure 3.3: Schematic view of the pn-junction of a silicon microstrip detector as used for the CMS Tracker, showing the n^+-type bottom layer, the n-type bulk and the implanted p-type strips. In addition the meaning of the pitch p and the width w are sketched.

This effect comes mainly from migration, recombination and annihilation of the additionally produced defects.

3.2.3 Charge Collection Efficency

Irradiation also decreases the charge collection efficiency, i.e. the ratio of charges produced by a traversing particle and the charge finally measured at the electrodes. This is due to the additionally introduced charge traps and recombination centers. Nevertheless, since the probability of charge trapping is proportional to the drift time, this effect can be compensated by applying a higher reverse bias voltage at the junction, in order to increase the drift velocity.
While the efficiency does not increase above the depletion voltage for non-irradiated structures, one has to apply much higher voltages in irradiated semiconductors to reach a plateu. In practice, this overbiasing beyond the depletion voltage in order to reach the efficiency plateu is limited by high voltage breakdown.

3.3 Sensor Design and Specifications

3.3.1 General Design

In the case of silicon microstrip sensors the pn-junction is typically realized by a n-type bulk and implanted p-type strips. The advantage of such a design in comparison to an ordinary diode lies in the spatial resolution due to the strips.
The resolution of such a geometry, using a simple readout system where the position information is derived from the strip with the highest signal, is given by (with p beeing the pitch of two neighboring strips):

$$\mathrm{RMS}_{\mathrm{strips}} = \frac{p}{\sqrt{12}} \tag{3.6}$$

This resolution can be significantly improved if the analog signals of all strips are readout. Since the charge, produced by a traversing particle, is shared between neighboring strips due to capacitive coupling, and due to the increase of the charge

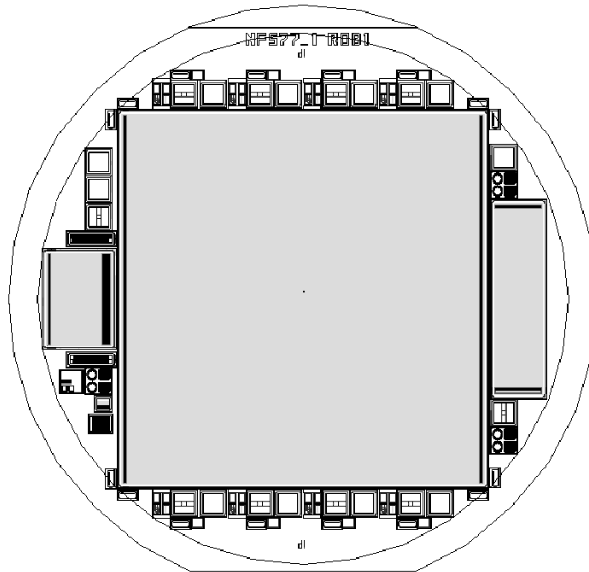

Figure 3.4: Schematic view of a processed 6”wafer (OB1 structure).

cloud’s width, caused by diffusion when traveling to the electrodes, signals are typically spread over several strips (so called *clusters*). By using for example a center of gravity algorithm one can get a more accurate estimate from such clusters for the particle’s crossing point.
The sensors for the CMS Silicon Microstrip Tracker are coated at the backplane with metallized n^+-type silicon, i.e. silicon with extremely high acceptor concentration, to guarantee the electric contact. On top of this structure is an insulating layer, consisting of SiO_2- and Si_3N_4-deposits, with Al-strips positioned directly above the p-type strips. From this capacitively coupled metal strips the (induced) signal is readout. Both the p-type and the metal strips have contact pads at their endings. The DC-pads, that are connected to the p-type strips, are only used for testing purposes (see chapter 4.2) while from the AC-pads, which are connected to the metal strips, the signals are readout.
The whole structure is surrounded by the so called bias line and the guard ring. The bias line, which is connected to the p-type strips, is the second electric contact that, together with the n^+-layer on the backplane, powers the junction. To seperate the strips from each other the bias line and the implanted strips are coupled via poly-silicon resistors. The guard ring achieves a homogenious voltage drop through the bulk even near to the edges. This prevents an increased leakage current caused by undesireable bendings of the fermi-levels near the cutting edges and facilitates the sensor’s stability.

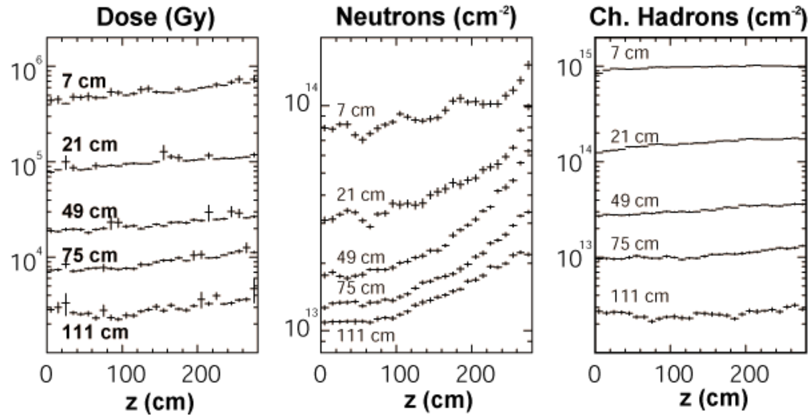

Figure 3.5: The expected fluences of photons, neutrons and charged particles in the CMS experiment over 10 years of operation as a function of the distance z from the collision point along the beamaxis and the radius r.

3.3.2 Specifications regarding the LHC Environment

The sensors have to be very radiation hard, due to the extreme particle fluence especially in the inner layers (see figure 3.5). Therefore various requirements, that reflect the results from extensive irradiation studies, were taken into account for the final sensor design [10]:

- Irradiation leads to the formation of trapped charges in the oxide and its interface to the bulk. This charge is mostly positive and therefore leads to the accumulation of an electron layer between the strips, which in turn increases the interstrip capacitance. A $\langle 1\,0\,0 \rangle$ crystal orientation of the bulk substrate offers less dangling bonds for trapping charges in comparison to other orientations. Thus it guarantees a significantly smaller increase of the interstrip capacitance due to irradiation. This is important for the sensor's noise figure (see chapter 7.2) and the effect of charge sharing.

- The depletion voltage is roughly proportional to the doping concentration of the bulk. Thus irradiation decreases the depletion voltage until the inversion point is reached. Afterwards, when the bulk is effectively p-type and the junction has therefore moved to the backplane, it increases again (compare to figure 3.2). This means, that an unirradiated sensor has to have a certain depletion voltage if it shall be operational after 10 years of LHC, since the maximum bias voltage is limited by the power supplies. On the other hand, a higher doping concentration increases the sensor's capacitance and hence decreases the signal-to-noise ratio (SNR). Therefore the substrate's resistivity ($\rho \propto N_{\text{eff}}^{-1}$) is $1.5 - 3.25\,\text{k}\Omega\,\text{cm}$ for sensors in the inner regions and about $4-8\,\text{k}\Omega\,\text{cm}$ for those in the outer regions. This ensures a sufficient SNR with a bias voltage not exceeding 400 V during LHC lifetime.

- The strip pitches of all sensors are in the range of 80-205 μm with a constant value of $w/p = 0.25$ to optimize the signal-to-noise performance, while maintaining good high voltage stability. Since a homogenious granularity

throughout the Tracker is desireable, the actual choice of the pitch depends on the sensors's distance from the collision point.

- The metal strips are 4-8 μm wider than the implant strips. This also improves the high voltage stability because this overhang shifts the high field gradients near the junction from the semiconducting material into the oxide layer which has a much higher breakdown voltage.

- Two different substrate thicknesses, i.e. 320 μm for the shorter sensors in the inner layers and 500 μm for the longer ones in the outer layers, where always two sensors are mounted on one module, will be used. This allows to compensate the increase in noise, due to longer strips, with a larger signal, owing to the increased charge collected in the thicker detectors.

The sensors are made from high resistivity 6" silicon wafers using the standard planar production process usually employed in the IC-industry. The outer parts that are not needed for the sensor itself, called half-moons because of their shape, host additional devices called *test structures* (see section 4.3). The thin sensors are supplied to the CMS Tracker Collaboration by HPK[2] and the thick sensors by STM[3].

3.4 Readout Electronics

The sensors are readout with 4 or 6 chips, depending on the number of strips. The *APV25 chips* [11], as the readout chips are called, are produced in a 0.25 μm CMOS process, are radiation hard and operate with low noise and power consumption. They have 128 channels, each consisting of a 50 ns CR-RC type shaping amplifier, a 192 element deep pipeline and a pulse shape processing stage which can implement a deconvolution operation in order to achieve a single bunch crossing resolution necessary at high luminosty. The analogue output samples are then multiplexed onto a single output for subsequent optical transmission to the DAQ system. The readout chip, together with the multiplexer and other devices, used mainly for the communication with the chip, are assembled on so called *hybrids*.
The chips can operate in one of three modes:

- *Peak mode*: Following an external trigger, one sample for each channel (timed to be at the peak of the amplifier output pulse shape) is read from the pipeline and then output through the multiplexer.

- *Deconvolution mode*: This will be the default operation mode for the experiment where the time between two bunch crossings (25 ns) is much less than the amplifier's shaping time [12, 13].
  Three samples per channel are read from the pipeline and then combined in a weighted sum before output in order to reconstruct the signal of a single event. The shaper output is sampled with the bunch crossing frequency and

[2]Hamamatsu Photonics K.K., Hamamatsu City, Japan
[3]ST Microelectronics, Catania, Italy

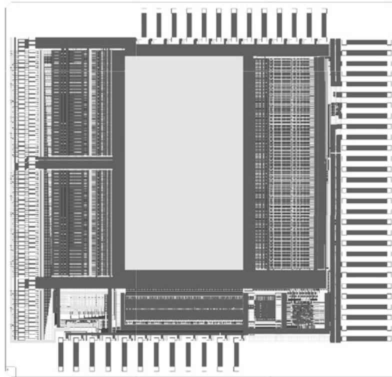

Figure 3.6: The APV25 chip.

stored in the pipeline. With the sampled shaper output values p_i and the weights w_i, the deconvoluted output d_k becomes:

$$d_k = w_3 p_{k-2} + w_2 p_{k-1} + w_1 p_k \tag{3.7}$$

It has been shown that this procedure is exact for an integrating preamplifier followed by a CR-RC shaper using the weights

$$w_1 = A\frac{\mathrm{e}^{x-1}}{x}, \quad w_2 = A\frac{-2\mathrm{e}^{-1}}{x} \quad \text{and} \quad w_3 = A\frac{\mathrm{e}^{-x-1}}{x} \tag{3.8}$$

with the ratio between sampling time and peaking time $x = T/T_\mathrm{p}$ and a normalisation factor A.

- *Multi-mode*: A sequence of external triggers allows a number of consecutive pipeline samples to be transmitted in consecutive output data frames.

The pipeline is used to store the amplifier outputs, sampled at the 40 MHz LHC frequency, while external trigger decisions are taken. The pipeline depth allows a programmable latency of up to 160 bunch crossings (4 μs). The APV25 chip contains all the necessary features, including on-chip bias and calibration pulse generation, and a slow control interface for programming these features and the operation mode of the chip.

3.5 Tracker Geometry

For the Tracker [6], the sensors and readout chips are assembled to $\sim$ 15000 modules, covering a total area of 206 m^2. They will be arranged in four subsystems called Tracker Inner Barrel (TIB), Tracker Outer Barrel (TOB), Tracker Inner Discs (TID) and Tracker End Caps (TEC) – see figure 3.7 and tables 3.1, 3.2 and 3.3 for details.

Depending on the position within the Tracker, the geometry of the sensors and the number of readout strips varies: In the barrel region, the sensors are rectangular, while the endcap sensors are of trapezoidal shape to fit together. To allow

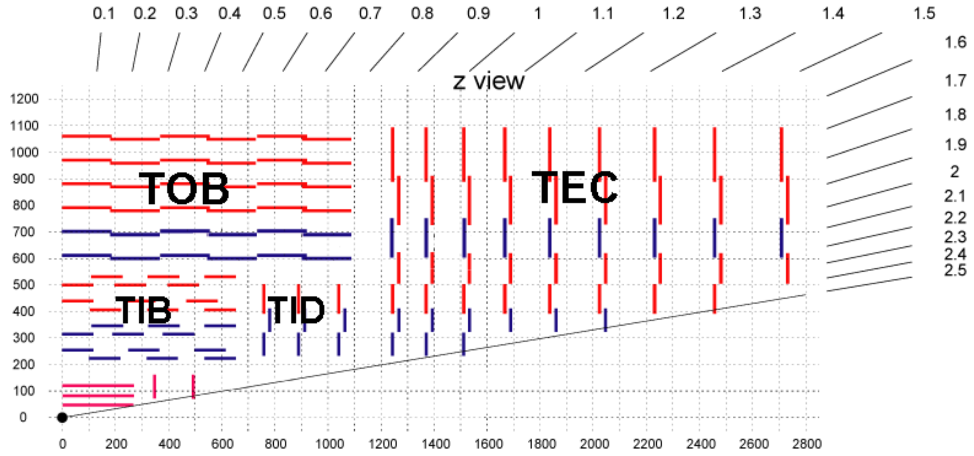

Figure 3.7: View of the CMS Tracker. Pixel layers are shown in pink, layers containing microstrip sensors are shown in red (single sided) and blue (double-sided).

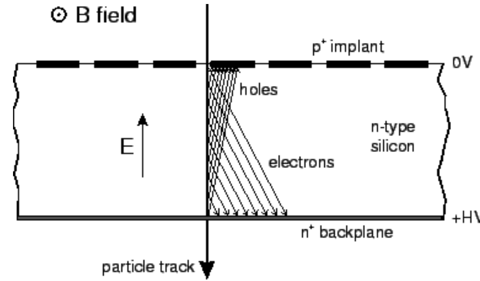

Figure 3.8: Electrons and holes are deflected under the influence of an magnetic field. This Lorentz shift causes an offset between the particle track and the measured position.

better area coverage in the barrel, the modules will overlap like roof tiles, which causes a tilt of 8° to 12°. This has even another positive effect: If a magnetic field perpendicular to the electric field is present, as it is the case in the bulk of barrel sensors, the charges are deflected from their track. This results in an inclined carrier movement relative to the electric field, whereas the electrons and holes are subject to different shifts, since their drift velocities are different (see figure 3.8). This *Lorentz shift* widens the electrode target area of the charge proportional to the detector thickness and the target center is offset relative to the traversing particle's track. By mechanically tilting the sensor, the target areas of the electrodes of both electrons and holes coincide. With this choice, the equal Lorentz shifts of both carriers can be easily corrected by a numerical offset subtraction.
For the overal angle specifications within the Tracker typically units of the pseudorapidity η are used, which is defined by:

$$\eta = -\ln\left(\tan\frac{\alpha}{2}\right) \quad (3.9a)$$

$$\frac{r}{z} = \tan\alpha \quad (3.9b)$$

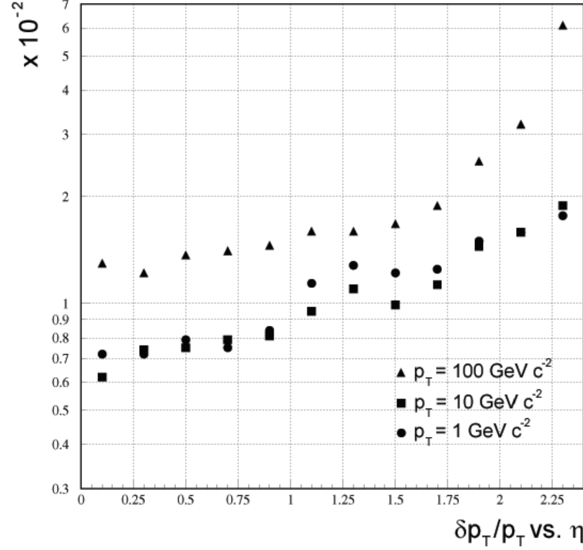

Figure 3.9: CMS Tracker stand-alone transverse momentum resolution as a function of η, for muons having $p_{\mathrm{T}} = 1$, 10 and 100 GeV c^{-2}.

The layout was optimized in order to fulfil all needed physics requirements. This means in detail:

- Isolated tracks with high p_{T} are reconstructed with a transverse momentum resolution of better than $\delta p_{\mathrm{T}}/p_{\mathrm{T}} \approx (15{\cdot}p_{\mathrm{T}} \oplus 0.5)\%$, with p_{T} in TeV c^{-2}, in the central region of $|\eta| \leq 1.6$, gradually degrading to $\delta p_{\mathrm{T}}/p_{\mathrm{T}} \approx (60{\cdot}p_{\mathrm{T}} \oplus 0.5)\%$, with p_{T} in TeV c^{-2}, as η approaches 2.5 (see figure 3.9). This resolution is well suited to the reconstruction of narrow states decaying into charged particles, and is sufficient to ensure reliable charge assignment for muons and electrons up to the highest kinematically accessible momenta.

- In combination with the outer muon chamber system, the muon momentum resolution above approximately 100 GeV c^{-2} can be parameterised as $\delta p/p \approx (4.5 \cdot \sqrt{p})\%$, with p in TeV c^{-2}, for rapidities extending up to at least $\eta = 2$. This results in a momentum resolution better than 10% even at 4 TeV c^{-2}.

- In dense jet environments, charged hadrons with p_{T} above 10 GeV c^{-2} are reconstructed with an efficiency approaching 95%, and even hadrons with p_{T} as low as 1 GeV c^{-2} are reconstructed with an efficiency better than 85%. The reconstruction efficiency for muons is better than 98% over the full η range, even for values of p_{T} as low as 1 GeV c^{-2}. High energy electrons are reconstructed with an efficiency above 90%.

- In the central rapidity region tagging efficiencies of 50% or better can be obtained for b-jets ranging from 50 GeV to 200 GeV E_{T}, with a mistagging probability of around 1% to 2%. In the forward rapidity region, for equal mistagging probability, the tagging efficiency remains around 40%.

type	length [mm]	height [mm]	pitch [μm]	strips	quantity
IB1	63.3	119.0	80	768	1536
IB2	63.3	119.0	120	512	1188

Table 3.1: Inner Barrel thin sensors, geometrical dimensions and multiplicities: IB1 will be mounted on 768 double-sided modules in the two inner layers of TIB, IB2 in 1188 single modules in the two outer layers.

type	length [mm]	height [mm]	pitch [μm]	strips	quantity
OB1	96.4	94.4	122	768	3360
OB2	96.4	94.4	183	512	7056

Table 3.2: Outer Barrel thick sensors, geometrical dimensions and multiplicities: OB1 will be mounted on 1860 single-sided modules in the layer 5 and 6 of TOB, OB2 in the inner TOB layers (1-4) in single- and double-sided modules. All TOB detectors will be composed of two daisy-chained sensors.

type	length [mm]	height [mm]	pitch [μm]	strips	quantity
W1 TEC	64.1-87.9	87.2	81-112	768	288
W1 TID	63.6-93.8	112.9	80.5-119	768	288
W2	88.1-112.2	90.2	113-143	768	864
W3	64.9-83.0	112.7	123-158	512	880
W4	59.7-73.2	117.2	113-139	512	1008
W5a	98.9-112.3	84.0	126-142	768	1440
W5b	112.5-122.8	66.0	143-156	768	1440
W6a	86.1-97.4	99.0	163-185	512	1008
W6b	97.5-107.5	87.8	185-205	512	1008
W7a	74.0-82.9	109.8	140-156	512	1440
W7b	82.9-90.8	98.8	156-172	512	1440

Table 3.3: Geometrical dimensions and multiplicities for thin (W1-W4) and thick (W5a-W7b) wedge sensors for TID and TEC: W1 has two different versions for TID and TEC, whereas TID shares identical W2 and W3 sensors with TEC. W1, W2 and W5 will be assembled in double-sided modules, the other geometries in single-sided modules.

Chapter 4

Qualification Procedures for the Silicon Microstrip Tracker

4.1 The Quality Assurence Scheme

The large number of sensors forced the CMS Collaboration to develop a quality assurance scheme [14] to ensure the full compliance of all delivered sensors with the technical specifications. Figure 4.1 shows the sensor flow during production between the involved laboratories. The contracts with the suppliers contain a comprehensive list of tests to be performed and corresponding acceptance criteria to be checked by the companies. It is the aim of these tests to ensure that at least 98% of the delivered and accepted sensors will later pass the CMS quality test.
After receiving and registrating sensors at CERN, the sensors and the corresponding test structures are shipped to the *Quality Test Centers* (QTC, see section 4.2). These five centers are responsoble for the overall quality since there the samples of sensors are fully characterised. A fixed percentage of test structures and some sensors will be shipped to the *Process Qualification Centers* (PQC, see section 4.3) where several properities concerning the production process are measured and long-term tests are done. Further test structures and sensors are sent to the *Irradiation Qualification Centers* (IQC). There the test structures become irradiated with neutrons and protons to ensure the required radiation hardness of the sensors. The adhesion of wire bonds (see section 4.4) is also checked using test structures at the laboratories responsible for module bonding.

4.2 Sensor Quality Control

In order to ensure the quality of the sensors used for the module construction, a detailed list of test to be performed by the QTCs has been defined.

4.2.1 Optical Inspection

The optical inspection consists in a survey by eye, an inspection under a microscope and a metrology of a few characteristic distances.

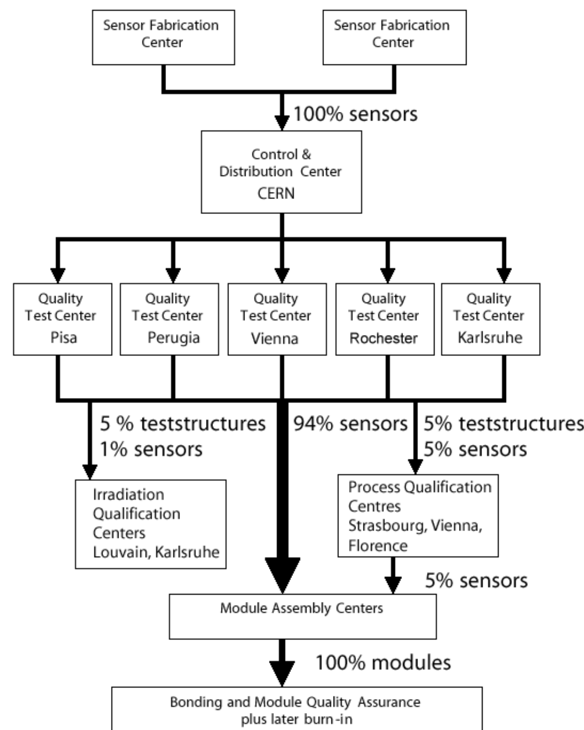

Figure 4.1: Sensor flow during production between the involved laboratories.

In the survey by eye firstly the packaging is checked for damages. Then the sensor is checked for big scratches, anomalous coloration or any evident defect. Afterwards, the sensor undergoes a detailed inspection of its edges under a microscope. The edges are a zone of potential fragility, where for instance during cutting or packaging breaks can occur, and are therefore of special interest. Large damages, defined as damages being bigger than 40 μm, can cause serious problems during operation. This includes injection of charge, a considerable increase of the leakage current or an instability in the electrical behaviour of the sensor. Finally, the precision of the cut is checked, measuring the distance between the edge and the active area at eight points near the four corners of the sensor. The precision required in the cut is 20 μm.

4.2.2 Electrical Characterization

The equipment required to perform the electrical characterisation consists of a computer controlled setup with a probe-station, a high voltage supply, an electrometer, a LCR-meter and a switching device.
Two main goals drove the design of the set-up for the electrical characterisation. Firstly, to automate and speed up the measurements as much as possible. Secondly, to touch sensors with probes as little as possible. In order to achieve the first goal, two different strategies have been adopted. The probe-stations in Perugia and Pisa are equipped with an automatic loader and pattern recognition software, that permits testing of sensors 24 hours per day without human intervention (up

to 25 sensors can be loaded in a single cassette). These probe-stations also use probe-cards, that permit to contact and test several strips (up to 29) at once, but need to ramp up and down the bias voltage when moving from one group of strips to another one. The probe-stations in Vienna, Karlsruhe and Rochester use single needles to contact the strips and one needle is attached to the chuck to contact the bias ring. Therefore it is not necessary to ramp up and down the voltage during the measurement of every strip. Both systems make a complete electrical test of a sensor in 3-4 hours (depending on the number of strips). The second goal has been reached by using a switching device, to which all instruments are connected. This permits to perform all measurements on every strip in sequence, such that each strip is contacted only once.
All parameters needed to perform the tests and the analysis are stored in an input file, which is centrally maintained at the Vienna QTC and, in case of agreed changes, re-distributed to all QTCs. The results of a quality control test of a sensor are written to a XML-file which is inserted into the CMS Tracker database (see section 4.5).
The electrical characterization consists of two global (IV, CV) and four strip-by-strip (I_{strip}, R_{poly}, I_{diel} and C_{AC}) tests. The electrical characterization is performed in a clean room with controlled temperature and humidity.

- IV: The total leakage current of the sensor from 0 V to 550 V reverse bias voltage is measured. The sensor is contacted at the backplane and the biasline, keeping the guard-ring floating, measuring with voltage steps of 5 V per second. The voltage dependent behaviour of the leakage current and its vlaue at 450 V are primarily used for characterizing a sensor (see chapter 6).

- CV: A measurement of the total capacitance of the sensor from 0 V to 350 V reverse bias voltage is perfomed. Thereby the capacitance is measured between the backplane and the biasline, keeping the guard ring floating, in steps of 5 V per second, at a frequency of 1 kHz. From this measurement it is possible to extract the depletion voltage of the sensor (see figure 4.2). Therefore the voltage, at which the capacitance reaches its minimum, has to be extracted by using a fitting-algorithm.

Strip-by-strip tests are performed at a bias voltage of 450 V in order to identify defective strips. The limit on the total number of defective strips per sensor is 1%. All four strip-by-strip tests are performed in the same scan, by contacting DC and AC pads simultaneously and by switching between different measurements.

- I_{strip}: The leakage current of each strip is measured in order to identify leaky strips, that exhibit a high noise. The limit on the strip current is 100 nA.

- R_{poly}: The value of each poly-silicon resistor connecting the strips to the bias line is measured. The acceptance criteria demand a value of $1.5 \pm 0.5\,\mathrm{M\Omega}$ for each strip, and an uniformity of 0.3 MΩ w.r.t. the average R_{poly} for all strips across the whole sensor.

- I_{diel}: This measurement is devoted to the identification of pinholes, i.e. defects in the dielectric layer that lead to an electric contact between the implant

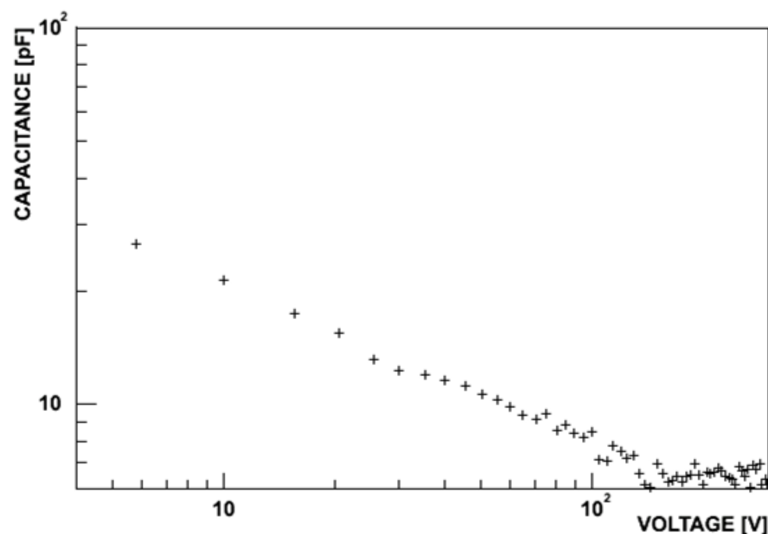

Figure 4.2: Typical CV-measurement of a silicon sensor. From a double-logarithmic diagram the depletion voltage can be easily extracted.

strips and the metal strips. By applying 10 V at the coupling capacitor of each strip the current across it can be measured. When the capacitor is good, the current equals the noise of the set-up (of the order of a pA). If I_{diel} exceeds 1 nA, the strip is classified as defective.

- C_{AC}: The value of the coupling capacitor for each strip is measured. This is again a check for pinholes and monitors the uniformity of the dielectric layer. The measurement is performed in such a way that it can also detect metal shorts between neighboring strips, since the capacitance is measured between two adjacent DC pads shorted together and the corresponding central AC pad. In that way shorted strips are measured as two capacitors in parallel and the resulting value is twice the correct one. The measurement is performed at a frequency of 100 Hz.

4.3 Process Control

The main purpose of the Process Control is to ensure a constant quality throughout the production and to detect any problem as soon as possible. This control is based on the characterisation of the test structures which are produced on the wafers' halfmoons together with the sensors. Their design is identical for all sensor geometries and suppliers and consist of nine devices (see figure 4.3):

- Ts-Cap: An array of 26 AC coupled strips, characterised by the same dielectric composition as the main sensor but directly connected to the bias line.
- Sheet: Composed of nine superficial structures to measure the sheet resistance. It consists of three implant strips, three Al-strips and three poly-silicon

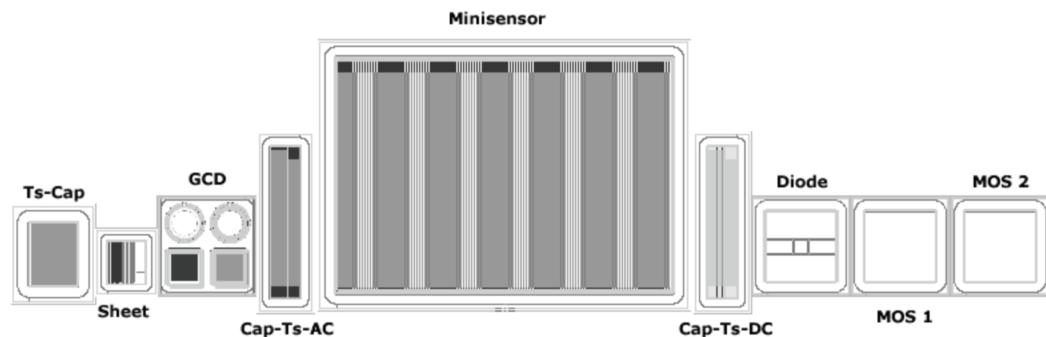

Figure 4.3: Layout of a standardized test structure.

resistors, all lying directly on the n-doped bulk.

- GCD: A set of four Gate Controlled Diodes, two circle-shaped and two square-shaped.
- Cap-Ts-AC: A device built of nine strips with the same structure as the main sensor. The three outermost strips on each side are connected through their metallisation to facilitate their grounding.
- Minisensor: A small-size replica of the main sensor. It has a rectangular shape and 192 strips with a pitch of 120 μm.
- Cap-Ts-DC: Similar to Cap-Ts-AC, except for the fact that the strips are not connected to the bias line, the dielectric layer is missing and the implanted strips can be contacted over their whole length.
- Diode: A simple diode surrounded by a guard ring.
- MOS 1 and MOS 2: For both the MOS devices included in the HPK structures and for the first MOS on STM wafers, the dielectric composition corresponds to the thick oxide layer in the interstrip region of the main sensor. In the second STM MOS the dielectric layer follows the structure of the metal strips' decoupling capacitance of the main sensor.

The process control on the test structures consists of the following measurements: CV on the MOS devices, CV on the diode, interstrip resistance between a central strip and its two first neighbours on Cap-Ts-DC, IV on the mini-sensor, interstrip capacitance between a central strip and its two closer neighbours on Cap-Ts-AC, IV on one of the square-shaped gate controlled diodes, the set of resistances of polysilicon resistors, Al-strips and p^+-strips on the sheet structure, six coupling capacitances in Ts-Cap, and finally the breakdown voltage of the decoupling capacitor oxide.
To contact all needed 49 pads on the test structure a probecard has been designed. The probecard output is connected via a switching matrix to the four measurement devices (LCR-meter, ampere meter and two voltage sources). In figure 4.4 a schematic of the electrical layout is shown. To avoid possible bad contacts, the

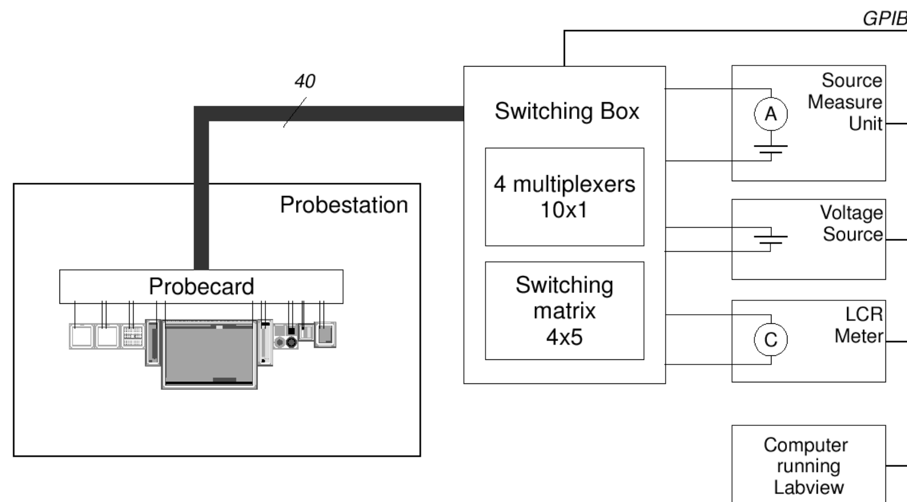

Figure 4.4: Schematic setup of a PQC probe-station

probes have been doubled each time it seemed useful. As mostly common equipment is used in the laboratories, a common software has also been adopted based on LabVIEW and made of three components: acquisition, analysis and database interface.

The acquisition part manages the ten measurements. The sequence of the measurements is done automatically but if needed, a single measurement can also be done manually. An emergency stop is implemented and if any current compliance is reached, the measurement is stopped.

After the measurements are performed, an analysis is needed to extract relevant parameters. This is the case for the flatband voltage of the MOS, the depletion voltage of the diode and the flatband voltage as well as the surface current of the gate controlled diode. All values are extracted using linear fits, which are used to find kinks between different linear regions.

All the measurements done are stored in the CMS Tracker Database (see section 4.5). The same procedure as used for QTC is adopted. All the parameters needed for the set of measurements come from an input file. At the end of the measurement series, an output file is produced in XML-format and inserted to the datatbase.

4.4 Module Assembly

Module assembly is performed in two steps: Firstly the sensors and the hybrids, which are connected to the so called pitch adapters (PA) in advance, are mounted on frames. This is done at the *Gantry Centers*. Afterwards the contacts between the PA and the (first) sensor and, in the case of two-sensor modules, between the first and the second sensor are connected. This second part is done at the *Bonding Centers*.

During the assembly at the Gantry Centers, i.e. gluing the various components on a frame, a fixed procedure has to be adhered. This includes for instance optical inspections of all components or an exact measurement of displacements of a sen-

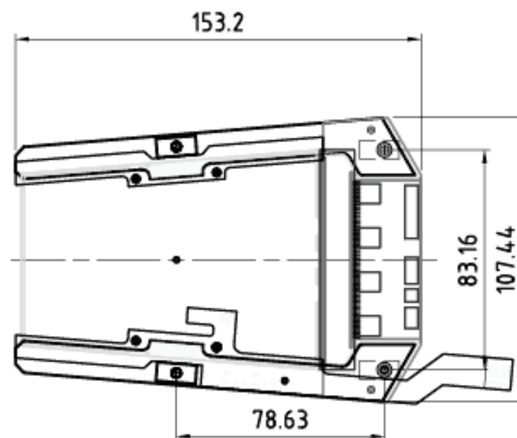

Figure 4.5: Sketch of a module frame for a wedge-shaped two-sensor module.

sor w.r.t. positioning marks on the frame. All relevant data has to be inserted into the database.
In the Bonding Centers the electrical contacts for the various components are established, using wire bonds. The thereby used wires are only a few tens of micrometers thick and are bonded on the contact pads using a technique similar to ultrasonic welding.
During and after assembly different tests have to be done. The most important (in the context of chapter 6 and 7) are the IV-tests: Firstly the IV-curve must be measured by bonding only to the bias line and the backplane, in order to assure, that the assembly so far has not deteriorated the performance of the sensors. After this measurement, the rest of the module should be bonded and the IV re-measured. The sensor bias current has to be ramped up to 450 V at a maximum rate of 10 V per second, whereas the bias current values should be recorded every 10 V. The relative humidity must be less than 30% during this and all subsequent measurements. In addition, again the hybrid has to be tested plus pulse shape tests, pedestal and noise tests (see chapter 7), pinhole tests, LED tests, pipeline tests and an optical inspections have to be done.
The readily assembled modules are finally graded: A module is Grade A if it has less than 1% bad channels (a channel with any testing failing). A module is Grade B if it has 1-2% bad channels. In both cases the module's IV-test has to pass the selection criteria (see below). Otherwise it will be marked as suspicious (grade C). Any module with more than 2% bad channels is graded F.
Regarding the IV-curve, the following conditions have to be met:

- $I(300\,V) < 5\mu A$ per sensor
- $I(450\,V) < 10\mu A$ per sensor
- $I_{measured}(300\,V) < 1.5 \cdot I_{database}(300\,V)$ (one-sensor modules)
- $I_{measured}(450\,V) < 1.5 \cdot I_{database}(450\,V)$ (one-sensor modules)
- $I_{measured}(300\,V) < 2 \cdot I_{database}(300\,V)$ (two-sensor modules)

- $I_{measured}(450\,V) < 2 \cdot I_{database}(450\,V)$ (two-sensor modules)

Thereby $I_{measured}$ is the bias current measured during the second IV-test and $I_{database}$ is the temperature compensated bias current from the sensor probing extracted from the database. The currents from the datatbase have to be compensated since the bias current is highly depending on the temperature. The formula for the compensation is (T given in Kelvin):

$$I(T) = I(T_0) \cdot (T/T_0)^2 \cdot e^{-7100 \cdot (1/T - 1/T_0)} \quad (4.1)$$

Again, all data, including the test results and the grading, have to be inserted into the datatbase.

4.5 The CMS Tracker Database

Two reasons led to the decision to implement a database: Firstly the huge amount of data due to the large number of sensors, modules and other components, plus the associated tests that have to be performed. Secondly the fact, that a lots of institutes, spread all over the world, which are working within the collaboration, have to have access to this data.
In addition to making data of various tests available, also all registrations and transfers of tracker components (reaching from module frames to support rods for the barrels) are recorded. This allows to organize and monitor the flow of equipment from the suppliers and within the collaboration.
For managing all this information, every component has an *object-ID* consisting of 14 digits, describing its functionality and origin. The object-ID of sensors includes for example information about its supplier (STM or HPK), its type and the day the wafer entered the production line.
The database is implemented as a SQL-database and is maintained by INPL[1]. To prevent misuse, either unintentional or even intentional, the database cannot be accessed directly, but all SQL-requests are preprocessed by a so called *relay-server*. In order to be still able to use the database comfortabely, a tool has been developed, the so called *BigBrowser*, that can be used by the whole collaboration. This java-based program allows to insert, view and extract data and runs on most platforms.

4.5.1 The visualDB-application

Nevertheless the BigBrowser-application, in spite of all upgrades, is not applicative for all kinds of data-processing. The need for a simple to use tool, for histograming and processing miscellaneous data, drove the development of the *visualDB*-application. This tool has been written in standard C++, using only the (almost standard) *libxml2*-library for XML-parsing and *ROOT*[2] for histograming and the graphical user interface, and is therefore portable to a big variety of platforms.

[1]Institut de Physique Nucleaire de Lyon, Universite Claude Bernard-Lyon
[2]CERN's official object-oriented data analysis framework

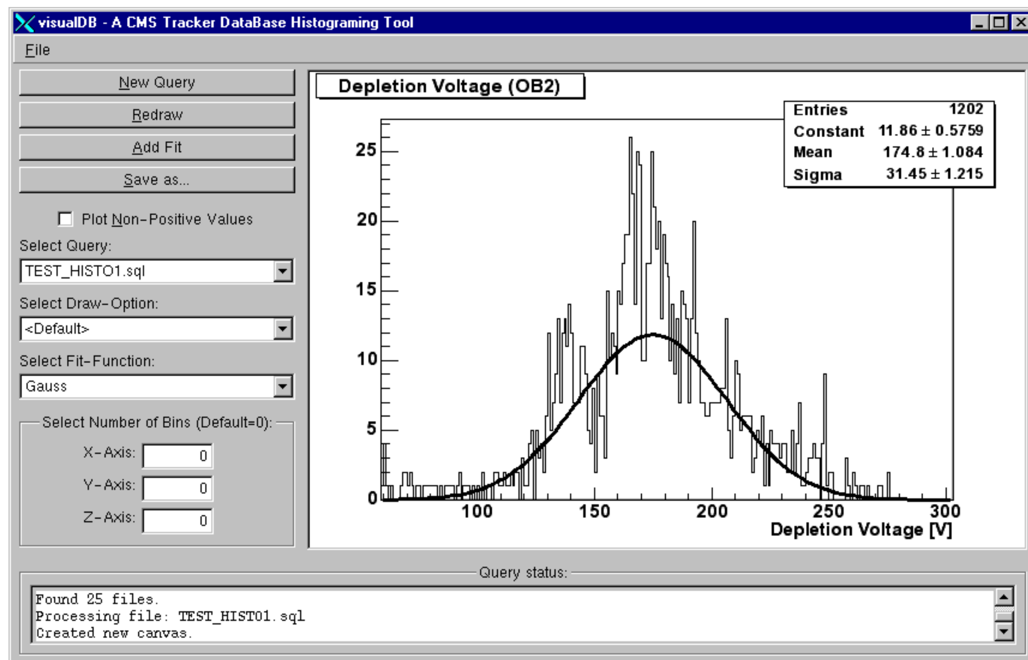

Figure 4.6: Screenshot of visualDB's graphical user interface.

The visualDB-application is able to create various histograms from all data-formats used within the database for storing numbers or dates. One-, two- and three-dimensional histograms are supported, including histograms with a time-like x-axis, where the dates can be extracted either from conventional date-entries or (for sensors) from the object-ID. Therefore only a simple SQL-query in pseudo-XML-format, as used for other database applications, has to be written and a small header, that tells the program what kind of histogram should be created, has to be added in front. The histograms can then be stored as graphic-files or ROOT-files for further processing.
In addition, four draw options and a text-field, showing the actual query-status, are available, fits can be added (Gaussian, Landau, exponential, linear, polynomial) and the number of bins can be defined by the user. Due to ROOT also greek-letters, mathematical symbols, superscripts and subscripts are available for axis labels and histogram titles.

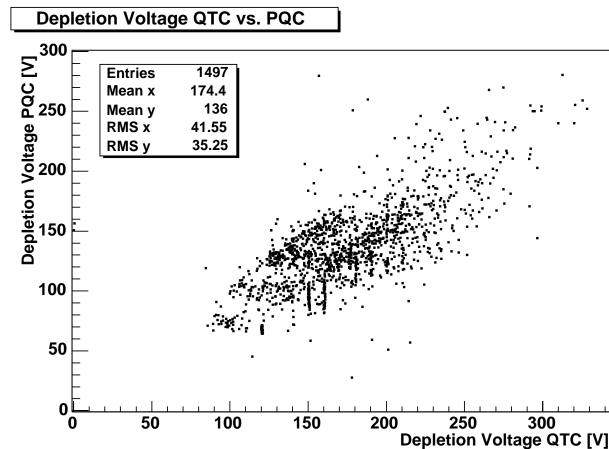

Figure 4.7: Graphical output from visualDB for below query.

```
#HISTO2 1 2 0 "Depletion Voltage QTC vs. PQC"
<select db="prod">
   qtc.V_DEPL_V AS "Depletion Voltage QTC [V]",
   pqc.V_DEPL AS "Depletion Voltage PQC [V]"
 FROM
   CVTEST_1_SEN_ qtc,
   TSCV_1_SEN_ qpc
 WHERE
   qtc.OBJECT_ID = pqc.OBJECT_ID AND
   qtc.STATUS = 'reference' AND
   pqc.STATUS = 'reference'
</select>
```

Figure 4.8: Example for a visualDB-query.

The header, i.e. the first line after the hash (#), defines the histogram type (HISTO2 - standard two-dimensional histogram), which columns of the result shall be used for histograming (values of column 1 for the x-axis and column 2 for the y-axis in this case - the third value tells the program that no z-axis is needed) and the histogram title.

Chapter 5

Teststructure and Sensor Depletion Voltages

5.1 Motivation

As described in section 4.3, the properties of a certain amount of teststructures are measured in order to ensure a constant quality of the produced sensors and to detect problems as soon as possible. Among these measurements also the depletion voltages of the planar teststructure diodes are determined. Since an appropriate value for the sensor's depletion voltage is essential to be operable after ten years of LHC, a reliable correlation between the depletion voltage of a teststructure diode (V_{diode}) and the corresponding sensor (V_{sensor}) is needed for sensible PQC-measurements. This became of special interest when HPK started to deliver sensors made of silicon having an unusual high resistivity, since the resistivity is monitored most comfortably via the depletion voltages of the teststructure diodes.
In a first attempt to find a theoretical description of this correlation [15], the geometry of a depleted microstrip sensor was modelled in the following way:

- The backplane consists of an ideal conducting plane,
- the depleted bulk is a charged dielectric with the dielectric constant ϵ, the space-charge density ϱ and the thickness d and
- on top is an infinite number of ideal conducting parallel srtips with pitch p and width w.

The diode was modelled similar only that an ideal conducting plane was atop the bulk instead of strips. Since the currents in a depleted bulk can be neglected in comparison to the space-charge density the problem can be treated electrostatic. Thereby V_{sensor} was defined as the voltage drop between one of the strips and the backplane which lead to:

$$V_{diode} = \frac{\varrho d^2}{2\epsilon_0 \epsilon} \tag{5.1a}$$

$$V_{sensor} = V_{diode} \left(1 + \frac{p}{\pi d} \frac{\epsilon}{\epsilon + 1} A_0 \left(\frac{w}{p} \right) \right) \tag{5.1b}$$

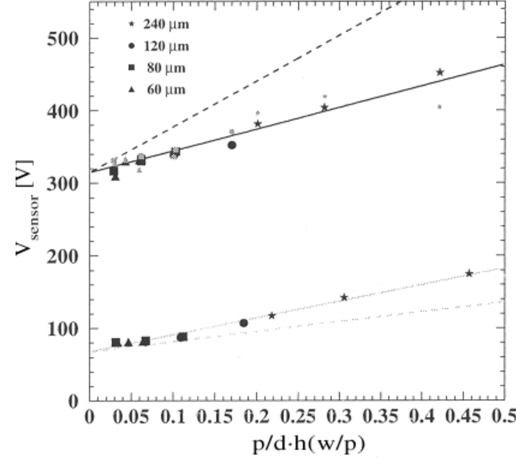

Figure 5.1: Depletion voltages for non-irradiated sensor-geometries with different pitches. Results for high resistivity sensors are shown in the lower part of the plot while those for the low resistivity ones in the upper part. The solid lines represent a linear fit of V_{sensor} as a function of the geometrical factor $\frac{p}{d} \cdot \mathrm{h}(\frac{w}{p})$ whereas the dashed line is the theoretical prediction from equation (5.3).

$$\mathrm{A}_0\left(\frac{w}{p}\right) = \frac{\sqrt{2}}{\pi} \int_0^{\pi\left(1-\frac{w}{p}\right)} \frac{x \sin \frac{1}{2}x}{\sqrt{\cos x + \cos \frac{w}{p}\pi}} \, \mathrm{d}x \tag{5.1c}$$

By using a fit, i.e.

$$\frac{1}{2\pi} \frac{\epsilon}{\epsilon + 1} \mathrm{A}_0(\xi) \equiv \mathrm{h}(\xi) \tag{5.2a}$$

$$\mathrm{h}(\xi) \cong -0.0011 \cdot \xi^{-2} + 0.059 \cdot \xi^{-1} + 0.24 - 0.65 \cdot \xi + 0.36 \cdot \xi^2 \tag{5.2b}$$

for silicon, this can be simplified to [16]:

$$\mathrm{V}_{\mathrm{sensor}} = \mathrm{V}_{\mathrm{diode}} \left(1 + 2\,\frac{p}{d}\,\mathrm{h}\left(\frac{w}{p}\right)\right) \tag{5.3}$$

Unfortunately this nice correlation, that depends only on the sensor's geometry, is not always working as good as desired. Figure 5.1 shows the results from a R&D-project that investigated different sensor designs [10].
In order to get an improved correlation it seems, that the investigated model for the sensor has to be improved. A possible improvement is to replace the ideal conducting strips with strips consisting of ordinary charged matter, representing the implant strips. This should in principle improve the results for two reasons:

1. The depletion voltage is the voltage drop between the sensor's backplane and the implanted p-type strips. Thus charged strips should be a better approximation for the physical situation in a pn-junction.

2. Since an electric field is always perpendicular to the surface of an ideal conductor, the shape of the electric field is not satisfyingly reproduced by using

conducting strips. The electric flux lines are in general not supposed to be bended towards the implanted strips, such that charged strips should reproduce the physical situation more realistic.

In this approximation depleted silicon microstrip sensors are treated as structures of n-type silicon bulks with a space-charge density $e\,n_+$ and thickness d covered by an ideal conductor on one side and an infinite number of charged strips of width w, pitch p and a surface charge σ on the other side. Analogous, for diodes simply the strips have to be replaced by a charged layer. The depletion voltage of the microstrip sensor V_{sensor} is thereby defined as the voltage drop between the backplane and the middle of a strip.

5.2 Theory

5.2.1 Basic Equations

In order to prevent the need to deal with induced charges at the surfaces of dielectrica, all calculations will treat the *electric displacement* $\vec{D}$, since it depends only on *free* charges. The Maxwell equations for the electrostatic case together with the material equation for dielectric matter, i.e.

$$\text{div}\vec{D} = \varrho \tag{5.4a}$$

$$\text{rot}\vec{E} = 0 \tag{5.4b}$$

$$\vec{D} = \epsilon_0\vec{E} + \vec{P} = \epsilon_0\epsilon\vec{E} \tag{5.4c}$$

lead to:

$$\text{div}\vec{D} = \varrho \tag{5.5a}$$

$$\text{rot}\vec{D} = 0 \tag{5.5b}$$

This can be rewritten as:

$$\vec{D} = -\text{grad}\,\phi_D \tag{5.6a}$$

$$\triangle\,\phi_D = -\varrho \tag{5.6b}$$

5.2.2 Potential of a Charged Bulk next to a Conductor

For the one-dimensional Poisson equation

$$\frac{\partial^2}{\partial x^2}\phi = -4\pi q(x) \tag{5.7}$$

the Greens-function reads:

$$G(x, x') = -2\pi|x - x'| \tag{5.8}$$

This leads to

$$\phi(x) = a(x)\,x + b(x) \tag{5.9}$$

with:

$$a(x) = 2\pi \int_{x}^{\infty} \mathrm{d}x' q(x') - 2\pi \int_{-\infty}^{x} \mathrm{d}x' q(x') \tag{5.10a}$$

$$b(x) = 2\pi \int_{-\infty}^{x} \mathrm{d}x'\, x' q(x') - 2\pi \int_{x}^{\infty} \mathrm{d}x'\, x' q(x') \tag{5.10b}$$

For a charged bulk with thickness d and a space-charge density like

$$\varrho(x) = \begin{cases} e\, n_+ & 0 < x < d \\ 0 & \text{else} \end{cases} \tag{5.11}$$

next to an ideal conducting plate at $x = 0$ the *effective* space-charge density, i.e. including all mirror charges, reads:

$$\varrho_{\text{eff}}(x) = \begin{cases} e\, n_+ \operatorname{sign}(x) & |x| < d \\ 0 & |x| > d \end{cases} \tag{5.12}$$

The corresponding potential (for the electric displacement) inside the bulk is then given by (using $q(x) = \varrho_{\text{eff}}(x)/4\pi$):

$$\phi_{\text{D,bulk}}(x) = \frac{e\, n_+}{2}(x - d)^2 \quad 0 < x < d \tag{5.13}$$

5.2.3 Potential of a Charged Plane next to a Conductor

For a charged plane at $x = d$ the space-charge density reads:

$$\varrho(x) = \sigma\delta(x - d) \tag{5.14}$$

In presence of an ideal conducting plate at $x = 0$ the *effective* space-charge density, i.e. including all mirror charges, gets:

$$\varrho_{\text{eff}}(x) = \sigma\,[\delta(x - d) - \delta(x + d)] \tag{5.15}$$

The corresponding potential (for the electric displacement) between the charged plane and the conductor is then given by (using equations (5.9) and (5.10a) as well as $q(x) = \varrho_{\text{eff}}(x)/4\pi$):

$$\phi_{\text{D,plane}}(x) = \sigma x \quad 0 < x < d \tag{5.16}$$

5.2.4 Potential of one Charged Strip

For the two dimensional Poisson equation

$$\triangle^{(2)}\, \phi = -4\pi q(\vec{x}) \tag{5.17}$$

the Greens-function reads:

$$G(\vec{x}, \vec{x}') = -\ln(|\vec{x} - \vec{x}'|^2) = -2\ln(|\vec{x}|) + \sum_{m \neq 0} \frac{2\pi}{|m|} F_m(\vec{x}')^* G_m(\vec{x}) \tag{5.18}$$

with

$$G_0(\vec{x}) = -2\ln(R), \tag{5.19a}$$

$$G_{m\neq 0}(\vec{x}) = \frac{1}{\sqrt{2\pi}} R^{-|m|} e^{im\varphi} \tag{5.19b}$$

$$F_m(\vec{x}) = \frac{1}{\sqrt{2\pi}} R^{|m|} e^{im\varphi} \tag{5.19c}$$

This leads subsequently to

$$\phi(\vec{x}) = \sum_m a_m(R) G_m(\vec{x}) + b_m(R) F_m(\vec{x}) \tag{5.20}$$

with:

$$a_0(R) = \int_0^R \mathrm{d}R'\, R' \int_0^{2\pi} \mathrm{d}\varphi' q(R'\varphi') \tag{5.21a}$$

$$a_{m\neq 0}(R) = \int_0^R \mathrm{d}R'\, R' \int_0^{2\pi} \mathrm{d}\varphi' \frac{2\pi}{|m|} F_m(R'\varphi')^* q(R'\varphi') \tag{5.21b}$$

$$b_0(R) = \sqrt{2\pi} \int_R^\infty \mathrm{d}R'\, R' \int_0^{2\pi} \mathrm{d}\varphi' (-2)\ln(R') q(R'\varphi') \tag{5.21c}$$

$$b_{m\neq 0}(R) = \int_R^\infty \mathrm{d}R'\, R' \int_0^{2\pi} \mathrm{d}\varphi' \frac{2\pi}{|m|} G_m(R'\varphi') q(R'\varphi') \tag{5.21d}$$

The space-charge distribution for a homogeniously charged strip of width w and with surface-charge $\sigma = 1$, perpendicular to the y-axis and infinitely long in z-direction can be written as:

$$\varrho\,(\vec{x}) = \Theta\left(\frac{w}{2} - |x|\right)\,\delta(y) = \frac{1}{R}\Theta\left(\frac{w}{2} - R\right)\left[\delta(\varphi) + \delta(\varphi - \pi)\right]. \tag{5.22}$$

This leads to (using $q(\vec{x}) = \varrho(\vec{x})/4\pi$):

$$\phi_{\,\mathrm{D,strip}} = \begin{cases} -\frac{w}{2\pi}\left(\ln\left(\frac{w}{2}\right) - 1\right) - \frac{R}{2}|\sin\varphi| + \frac{w}{4\pi}\sum\limits_{m=1}^{\infty} \frac{1}{m-2m^2}\left(\frac{2R}{w}\right)^{2m}\cos(2m\varphi) & R < \frac{w}{2} \\ -\frac{w}{2\pi}\ln(R) + \frac{w}{4\pi}\sum\limits_{m=1}^{\infty} \frac{1}{m+2m^2}\left(\frac{w}{2R}\right)^{2m}\cos(2m\varphi) & R > \frac{w}{2} \end{cases} \tag{5.23}$$

5.2.5 Depletion Voltage of a Planar Diode

The depletion voltage of a planar diode V_{diode} consisting of a n-type bulk of thickness d and space-charge density $e\,n_+$, a very thin p-type layer (represented by a

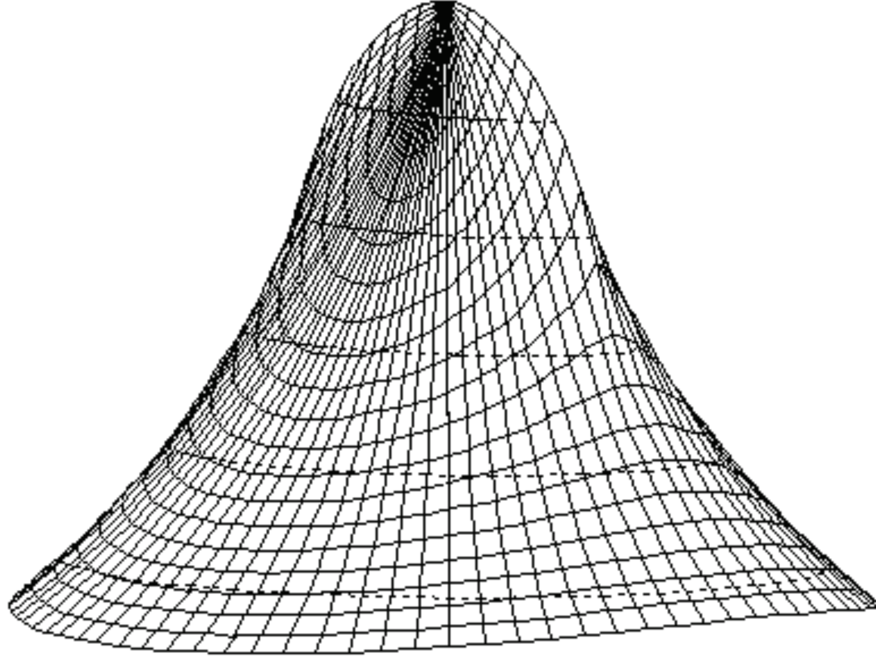

Figure 5.2: Potential of one charged strip.

plane at $x = d$ and with surface-charge σ) and an ideal conductor at $x = 0$ is given by:

$$\mathrm{V_{diode}} = \mathrm{V_{bulk}} + \mathrm{V_{plane}} \tag{5.24}$$

with:

$$\mathrm{V_{bulk}} = \frac{1}{\epsilon_0\epsilon}\,\Delta\phi_{\,\mathrm{D,bulk}} = \frac{1}{\epsilon_0\epsilon}\,(\phi_{\,\mathrm{D,bulk}}(d) - \phi_{\,\mathrm{D,bulk}}(0)) = \frac{e\,n_+}{2\epsilon_0\epsilon}\,d^2 \tag{5.25a}$$

$$\mathrm{V_{plane}} = \frac{1}{\epsilon_0\epsilon}\,\Delta\phi_{\,\mathrm{D,plane}} = \frac{1}{\epsilon_0\epsilon}(\phi_{\,\mathrm{D,plane}}(d) - \phi_{\,\mathrm{D,plane}}(0)) = \frac{\sigma}{\epsilon_0\epsilon}\,d \tag{5.25b}$$

This finally leads to:

$$\mathrm{V_{diode}} = \frac{e\,n_+}{2\epsilon_0\epsilon}\,d^2 + \frac{\sigma}{\epsilon_0\epsilon}\,d \tag{5.26}$$

5.2.6 Depletion Voltage of a Microstrip Sensor

The depletion voltage of a microstrip sensor $\mathrm{V_{sensor}}$ consisting of a n-type bulk of thickness d and space-charge density $e\,n_+$, an infinite number of very thin p-type strips (represented by strips with width w, the center at $x = 0, y = \pm nd$ and surface-charge σ) and an ideal conductor at $x = d$ is given by:

$$\mathrm{V_{sensor}} = \mathrm{V_{bulk}} + \mathrm{V_{strips}} \tag{5.27}$$

with:

$$\mathrm{V_{bulk}} = \frac{1}{\epsilon_0\epsilon}\,(\phi_{\,\mathrm{D,bulk}}(0) - \phi_{\,\mathrm{D,bulk}}(d)) = \frac{e\,n_+}{2\epsilon_0\epsilon}\,d^2 \tag{5.28a}$$

$$\mathrm{V_{strips}} = \frac{1}{\epsilon_0\epsilon}(\phi_{\,\mathrm{D,all\,strips}}(x{=}0, y{=}0) - \phi_{\,\mathrm{D,all\,strips}}(x{=}d, y{=}0)) \tag{5.28b}$$

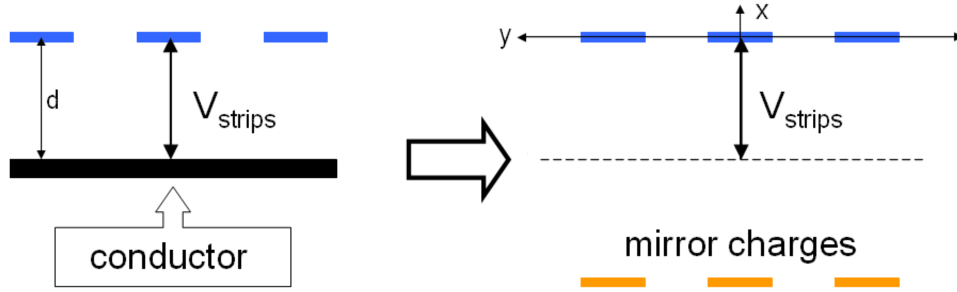

Figure 5.3: Alignment of the charged strips and the corresponding mirror charges.

Note in above equation that the potential of all strips together is constant for $x = d$ due to the conductor and that it is assumed that there is the center of a strip at $x=0$, $y=0$ (see figure 5.3).
The potential of all strips together $\phi_{\mathrm{D,all\,strips}}$ is the sum of the potentials of all strips with surface-charge σ at the positions $x=0$, $y=\pm nd$ and the corresponding *mirror charge strips* with surface-charge $-\sigma$ at the positions $x=2d$, $y=\pm nd$. Due to the mirror charges one can conclude that $\phi_{\mathrm{D,all\,strips}}(x=d, y=0)=0$ which, when ignoring the infinite series for $R > \frac{w}{2}$ that almost vanish for radii bigger than $\sim 3w$, leads to:

$$\begin{aligned}
\frac{\epsilon_0 \epsilon}{\sigma} \mathrm{V}_{\mathrm{strips}} &= \phi_{\mathrm{D,strip}}(x=0, y=0) - \phi_{\mathrm{D,strip}}(x=2d, y=0) + \\
&\quad + \sum_{n \neq 1} \left[\phi_{\mathrm{D,strip}}(x=0, y=np) - \phi_{\mathrm{D,strip}}(x=2d, y=np) \right] \qquad (5.29a) \\
&\simeq -\frac{w}{2\pi} \left[\ln\left(\frac{w}{2}\right) - 1 \right] + \frac{w}{2\pi} \ln(2d) + \\
&\quad + 2 \sum_{n=1}^{\infty} \left[-\frac{w}{2\pi} \ln(np) + \frac{w}{2\pi} \ln\left(\sqrt{4d^2 + n^2 p^2}\right) \right] \qquad (5.29b) \\
&= \frac{w}{2\pi} - \frac{w}{2\pi} \ln\left(\frac{w}{4d}\right) + \frac{w}{2\pi} \sum_{n=1}^{\infty} \ln\left(1 + \frac{4d^2}{n^2 p^2}\right) \qquad (5.29c)
\end{aligned}$$

The last infinite series can be calculated as follows:

$$\begin{aligned}
f(a) &= \sum_{n=1}^{\infty} \ln\left(1 + \frac{a}{n^2}\right) = \sum_{n=1}^{\infty} f_n(a) = \int_0^a \mathrm{d}a' \left[\frac{\mathrm{d}}{\mathrm{d}a'} \sum_{n=1}^{\infty} f_n(a') \right] + \underbrace{f(0)}_{=0} \\
&= \int_0^a \mathrm{d}a' \left[\sum_{n=1}^{\infty} \frac{\mathrm{d}f_n(a')}{\mathrm{d}a'} \right] = \int_0^a \mathrm{d}a' \left[\sum_{n=1}^{\infty} \frac{1}{a' + n^2} \right]
\end{aligned} \qquad (5.30)$$

Using the relation

$$\sum_{n=1}^{\infty} \frac{1}{a' + n^2} = \frac{1}{2a'} \left[\sqrt{a'}\pi \coth\left(\sqrt{a'}\pi\right) - 1 \right] \qquad (5.31)$$

yields after resubstitution:

$$f(a) = \ln\left[\frac{\sinh\left(\sqrt{a}\pi\right)}{\sqrt{a}\pi} \right] \qquad (5.32)$$

Finally one gets:

$$\mathrm{V_{sensor}} = \frac{e\,n_+}{2\epsilon_0\epsilon}\,d^2 + \frac{\sigma}{\epsilon_0\epsilon}\frac{w}{2\pi}\left\{1 + \ln\left[\frac{2}{\pi}\frac{p}{w}\sinh\left(2\pi\frac{d}{p}\right)\right]\right\} \tag{5.33}$$

5.2.7 Comparison between Sensor and Diode Depletion Voltages

For a sensor and a diode, with equal doping concentrations for the bulk as well as same concentrations in the implanted strips or the p-layer respectively (represented by the corresponding σ) and thickness d, one gets from equations (5.26) and (5.33):

$$\mathrm{V_{sensor}} = \mathrm{V_{diode}} - \frac{\sigma d}{\epsilon_0\epsilon}(1 - f(p, w, d)) \tag{5.34a}$$

with

$$\begin{aligned} f(p, w, d) &= \frac{1}{2\pi}\frac{w}{d}\left\{1 + \ln\left[\frac{2}{\pi}\frac{p}{w}\sinh\left(2\pi\frac{d}{p}\right)\right]\right\} \\ &\simeq \frac{1}{2\pi}\frac{w}{d}\left[1 + 2\pi\frac{d}{p} + \ln\left(\frac{1}{\pi}\frac{p}{w}\right)\right] \end{aligned} \tag{5.34b}$$

5.3 Results

Unfortunately the doping concentrations of neither the bulk nor the implant strips, which is proportional to σ, are measured during process or quality control. Nevertheless it is possible to compute an approximate value by using the average inverse diode resistivity $\overline{\rho_{\mathrm{d}}^{-1}}$, which is proportional to the doping concentration ($\mu_{\mathrm{e}} e\,\overline{n}_+ = \overline{\rho^{-1}}$), and the average depletion voltages $\overline{\mathrm{V}}_{\mathrm{diode}}$ of the teststructure diodes (see equation (5.26)):

$$\frac{d}{\epsilon_0\epsilon}\overline{\sigma} = \overline{\mathrm{V}}_{\mathrm{diode}} - \frac{d^2}{2\epsilon_0\epsilon\mu_{\mathrm{e}}}\overline{\rho_{\mathrm{d}}^{-1}} \tag{5.35}$$

Note that the right side of above equation uses only (more or less precisely) known quantities. The average diode depletion voltage can be computed from the available QTC-results, while the average inverse resistivity is monitored by the sensor suppliers during production.
In addition, the ratio $\beta = p/d$ is not constant for TID- and TEC-sensors, which are due to the detector geometry wedge-shaped. To regard this, one can rewrite equation (5.34b) with respect to $\alpha = p/w$ and β:

$$g\,(\alpha, \beta) = f\left(p, w = \frac{p}{\alpha}, d = \frac{p}{\beta}\right) = \frac{1}{2\pi}\frac{\beta}{\alpha}\left(1 + \ln\frac{\alpha}{\pi}\right) + \frac{1}{\alpha} \tag{5.36}$$

Averaging this expression yields:

$$\overline{g(\alpha,\beta)} = \frac{1}{\beta_{\text{max}} - \beta_{\text{min}}} \int_{\beta_{\text{min}}}^{\beta_{\text{max}}} \mathrm{d}\beta' g(\alpha,\beta') = g(\alpha,\overline{\beta}) \tag{5.37a}$$

$$\overline{\beta} = \frac{\beta_{\text{max}} - \beta_{\text{min}}}{2} \tag{5.37b}$$

The quality of a correlation is thereby measured via the merit function Δ:

$$\Delta^2 = \frac{1}{\mathrm{N_s}} \sum_{\mathrm{N_s}} \left(\mathcal{V}_{\text{sensor}} - \mathrm{V}_{\text{sensor}}(\mathcal{V}_{\text{diode}}) \right)^2 \tag{5.38}$$

In above equation $\mathcal{V}_{\text{sensor}}$ and $\mathcal{V}_{\text{diode}}$ are the measured PQC-values for the sensor's and the teststructure diode's depletion voltage. $\mathrm{V}_{\text{sensor}}$ is the theoretical value for the sensor's depletion voltage w.r.t $\mathcal{V}_{\text{diode}}$, including, in the case of the new correlation, also the inaccuracy due to the estimation in equation (5.35). Thereby $\mathrm{N_s}$ is the number of measured sensors. Since the accuracy of this approach depends highly on the available statistics, only sensor types where at least 30 measurements have been done were considered.
In addition it could be outruled, that the results from the QTC-measurements regarding the depletion voltage are biased by a systematic error. Since the CV-curve of a sensor depends on the frequency of the probing signal of the LCR-meter it was proposed, that this could influence the result of the fitting procedure for the extraction of the depletion voltage. Figure 5.4 shows the result of a series of measurements, done at the QTC-setup in Vienna. Only for small frequencies, i.e. around 500 Hz and below, the result shows a dependency, which is however negligible. Only for very high frequencies about 20 kHz the fitting procedure had to be altered slightly, since there the CV-dependence changes drastically for small voltages, such that this region had to be excluded from the fit.

5.3.1 Correlation for HPK-Sensors

In reality the assumption of a constant doping concentration, or resistivity respectively, across a wafer is not fulfilled, due to the production process of the ingots, from which the wafers are cut. For ingots used by HPK the radial distribution of the resistivity of wafers, cut from different positions on the ingots, is measured. A compilation of the results from 28 samples from two different ingots can be seen in figure 5.5, where the average inverse resistivity in dependence on the distance from the wafer's center is shown. Fitting this data yields:

$$\overline{\rho^{-1}_{\text{HPK}}}(r)\ [\mathrm{M\Omega^{-1}cm^{-1}}] = 464.43 - 0.54 \cdot r^2 - 0.056 \cdot r^4 \tag{5.39}$$

Note that in above equation r is the distance from the wafer's center in cm.
By assuming, that the resistivity does not change during the processing of the wafers and that the resistivity measurements have no relevant systematical error, one can use equation (5.39) to calculate a realistic value for the diode's resistivity

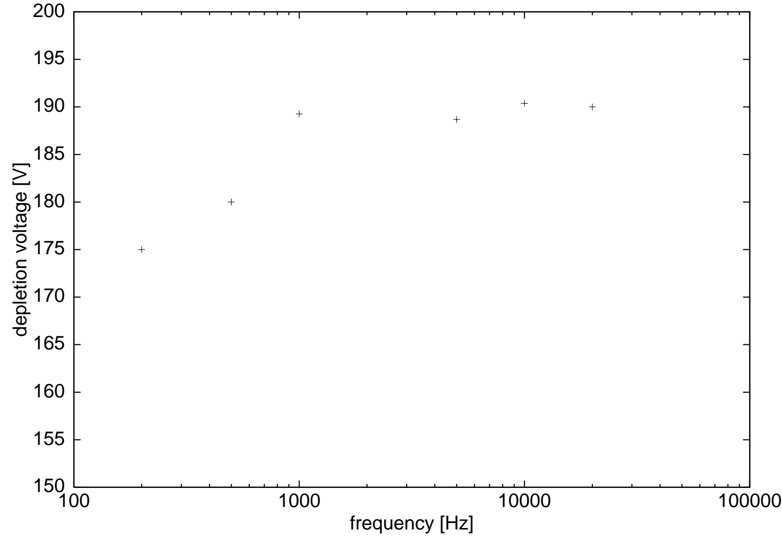

Figure 5.4: Measured depletion voltage of a W5A sensor in dependence on the frequency of the LCR-meter probing signal.

$\overline{\rho_{\mathrm{d}}^{-1}}$. By this, the different positions of the diodes for the various sensor designs can be taken into account. Inserting $\overline{\rho_{\mathrm{d}}^{-1}} = \overline{\rho_{\mathrm{HPK}}^{-1}}\,(r\!=\!r_{\mathrm{diode}})$ into equation (5.35) yields an approximate value for σ.
For the correlation between $\mathrm{V}_{\mathrm{diode}}$ and $\mathrm{V}_{\mathrm{sensor}}$ in equation (5.34a) this has an additional effect: The effective resistivity $\rho_{\mathrm{s,\,eff}}$ of a sensor corresponds to the maximum doping concentration, since the applied voltage has to be able to deplete the whole structure.

$$\rho_{\mathrm{s,\,eff}}^{-1} = \mu_{\mathrm{e}} e n_{+,\,max} \tag{5.40}$$

Thus the average ratio η between a sensor's average inverse effective resistivity and a diode's average inverse resistivity is given by:

$$\eta = \frac{\overline{\rho_{\mathrm{s,\,eff}}^{-1}}}{\overline{\rho_{\mathrm{d}}^{-1}}} = \frac{\overline{\rho_{\mathrm{HPK}}^{-1}}\,(r\!=\!0)}{\overline{\rho_{\mathrm{HPK}}^{-1}}\,(r\!=\!r_{\mathrm{diode}})} \tag{5.41}$$

Inserting this into equations (5.26) and (5.33) then yields a correlation that takes the inhomogenious resistivity distribution into account:

$$\mathrm{V}_{\mathrm{sensor}} = \eta\,\mathrm{V}_{\mathrm{diode}} - \frac{\sigma d}{\epsilon_0 \epsilon}(\eta - f(p,w,d)) \tag{5.42}$$

5.3.2 Correlation for STM-Sensors

For ingots used by STM only the average inverse resistivity is known approximately. From a sample of 68 ingots, whereas the data comes directly from the supplier[1], a value of

$$\overline{\rho_{\mathrm{STM}}^{-1}} = 189.75\ \mathrm{M}\Omega^{-1}\mathrm{cm}^{-1} \tag{5.43}$$

[1]Wacker Siltronic, Burghausen, Germany

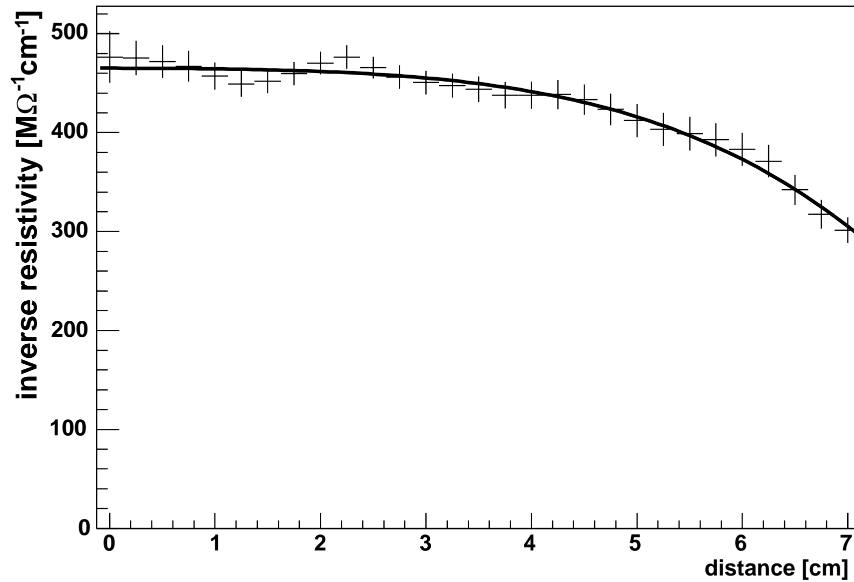

Figure 5.5: Radial distribution of the average inverse resistivity for wafers used by HPK. The corresponding resistivities are $\simeq 2.2\,\mathrm{k}\Omega\,\mathrm{cm}$ at $r = 0$ cm and $\simeq 3.5\,\mathrm{k}\Omega\,\mathrm{cm}$ at $r = 7$ cm respectively.

has been computed. Thus the inhomogenious distribution of the resistivity across the wafer cannot be regarded and instead of the corrected correlation (5.42) one has to use equation (5.34a).

5.3.3 Conclusion

Although the theoretical correlation presented above is based on very ideal assumptions, like for instance a homogenious doping concentration in the bulk, parallel strips and an infinite expanse, which are in general not met, a good agreement with the measurements could be accomplished. Especially the corrections due to the radial resistivity distribution for HPK sensors lead to a more realistic description of the actual results. Especially when regarding the uncertainties of the production parameters, i.e. the doping concentrations of the bulk material and the implant strips, this agreement is remarkable. Also a systematic error of the QTC-measurements, due to the LCR-meter probing signal frequency, which would of course influence this correlation, could be outruled.
Finally, since the theoretical correlation is reasonably confirmed by the experiment, it could be proved, that HPK was using silicon with a too high resistivity for several sensor batches, such that the affected sensors are not usable for the CMS Tracker.

Example for rectangular HPK-sensors: IB1

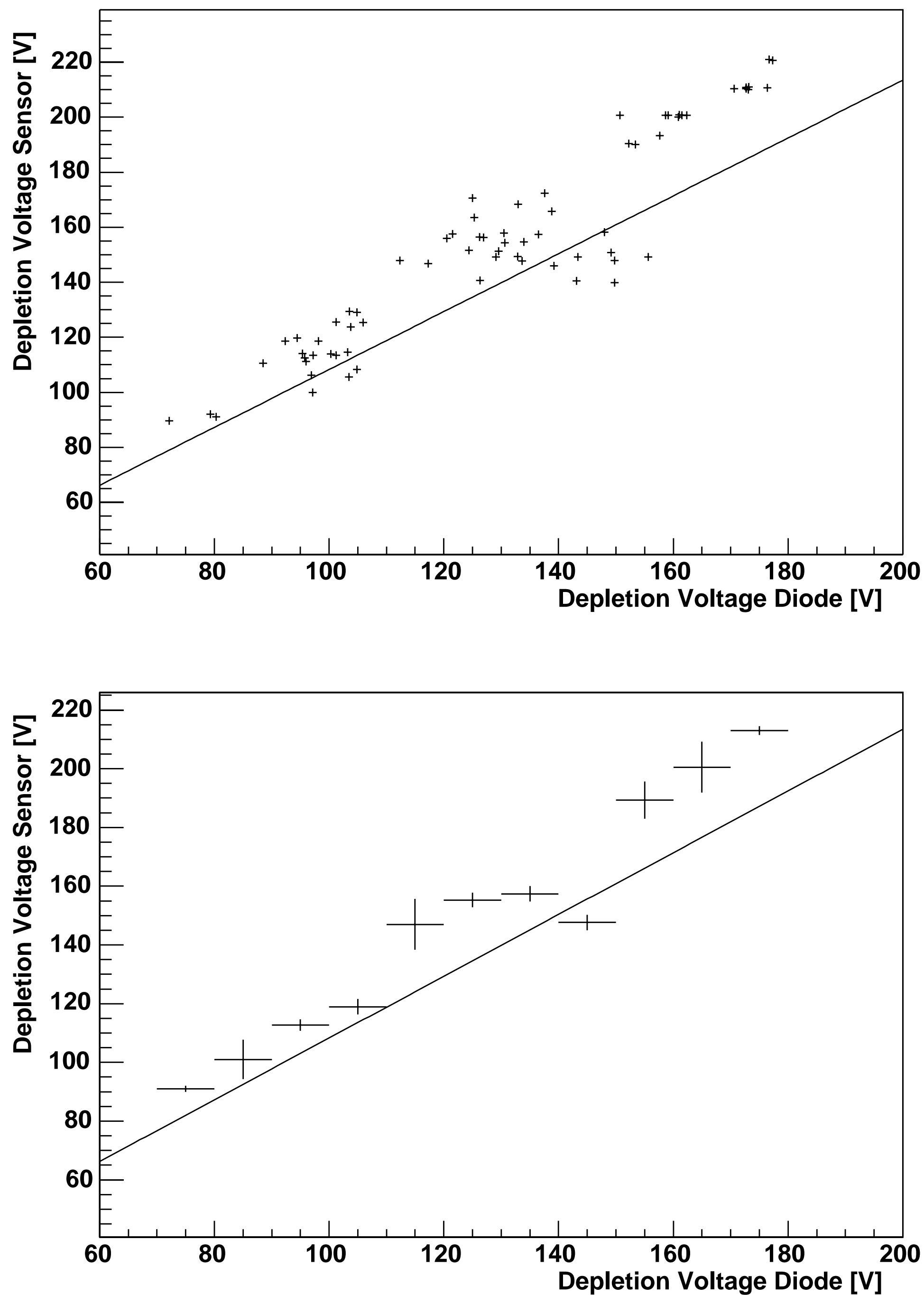

Figure 5.6: Results for IB2-sensors from HPK.

Above a scatter plot of all entries can be seen, showing the big spread within the distribution of the depletion voltages for one type of sensor, coming mainly from fluctuations of the resistivity of the ingots and the implanted strips. From the histogram below, showing the average for each bin as well as its variance, one can conclude that for IB2 the theoretical correlation (solid line) is very close to the measured one.

Example for wedge-shaped STM-sensors: W5B

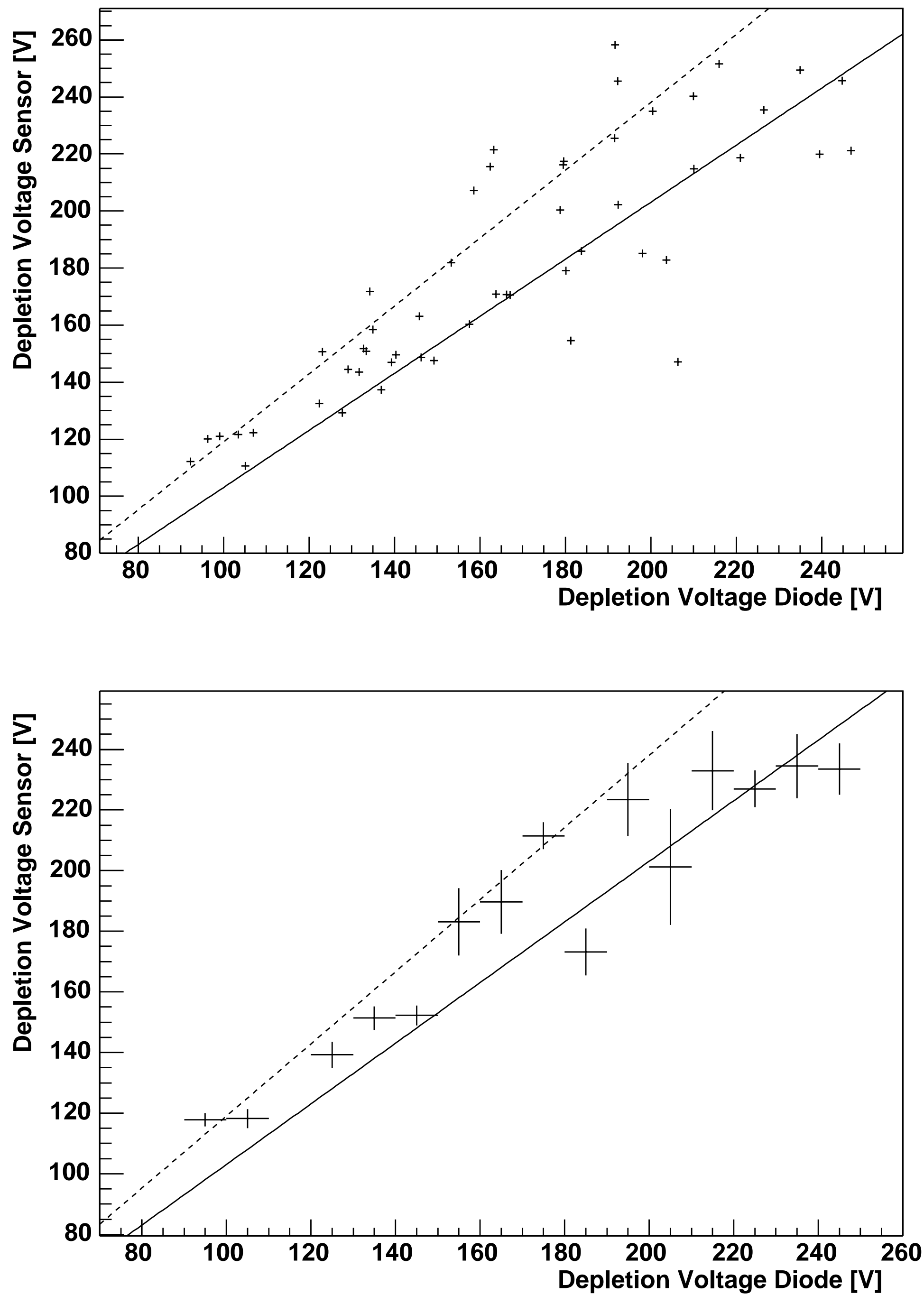

Figure 5.7: Results for W5B-sensors from STM.

Again a big spread of the depletion voltages, mainly due to fluctuations of the resistivity of the ingots and the implanted strips, can be seen in the scatter plot. Here in addition to the new correlation (solid line) also the older one (dashed line) is shown ($\Delta^2_{\mathrm{old}} = 942.6\,\mathrm{V}^2$, $\Delta^2_{\mathrm{new}} = 648.7\,\mathrm{V}^2$).

5.4 Sensor Pairing

For modules containing two sensors it was necessary to introduce sensible rules for chosing which sensors are mounted together. The depletion voltages of both sensors should be approximately the same, since a big difference would lead to an unnecessary high overdepletion and hence strain of one sensor. In addition this would cause a higher power consumption of the HV-supplies as needed.
One also has to bear in mind, that the depletion voltage of a sensor depends on the absorbed radiation dose. Apart from introducing new impurities and defects within the bulk the traversing particles also remove the existing donors. Even if this effect is qualitatively understood, the quantitative removal rate is yet not known. Therefore both extreme cases, i.e. without and with full donor removal, have been investigated. In addition the anneling of the sensors during attendance periods has to be taken into account. However, even in a worst case scenario the difference of both depletion voltages stays constant (see figures 5.8 and 5.9, provided by A. Furgeri, Universität Karlsruhe). Thus, when looking on the QTC-data of the accepted sensors used for two-sensor modules (see page 55) it was proposed to

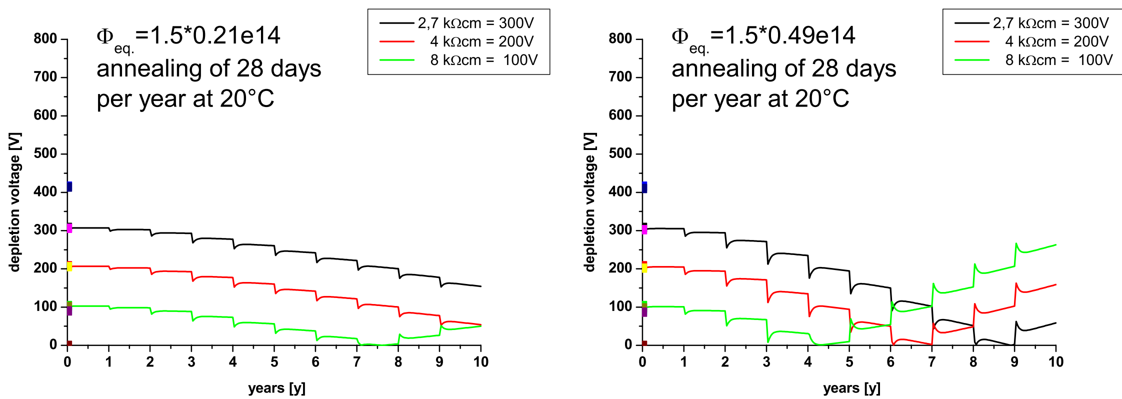

Figure 5.8: Predicted evolution of the depletion voltage for sensors with different resistivities without donor removal. The fluences correspond to the radiation levels expected for the inner and outer layers.

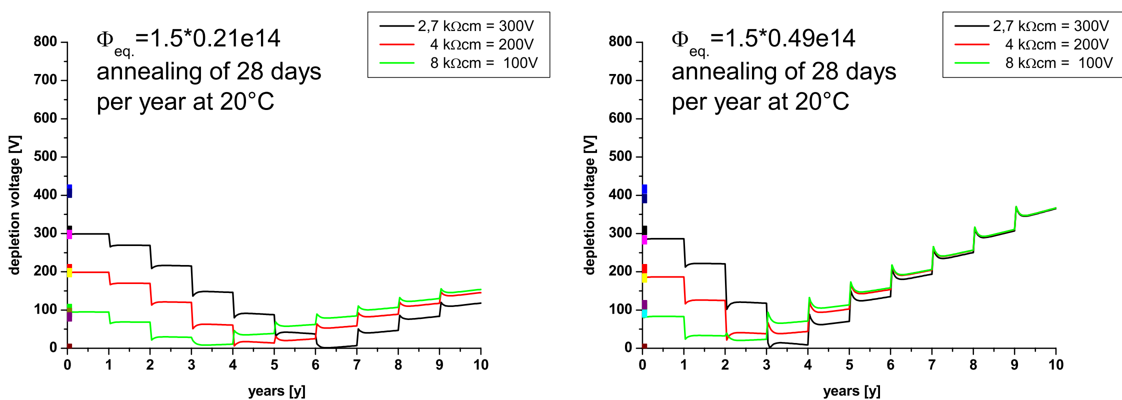

Figure 5.9: Predicted evolution of the depletion voltage for sensors with different resistivities with full donor removal. The fluences correspond to the radiation levels expected for the inner and outer layers.

mount only two sensors together when both have a depletion voltage between either 100 V and 200 V or 200 V and 300 V. This proposal has been accepted by the CMS Tracker collaboration at the Tracker Week in February 2004 at CERN and is by now applied at the Gantry Centers.

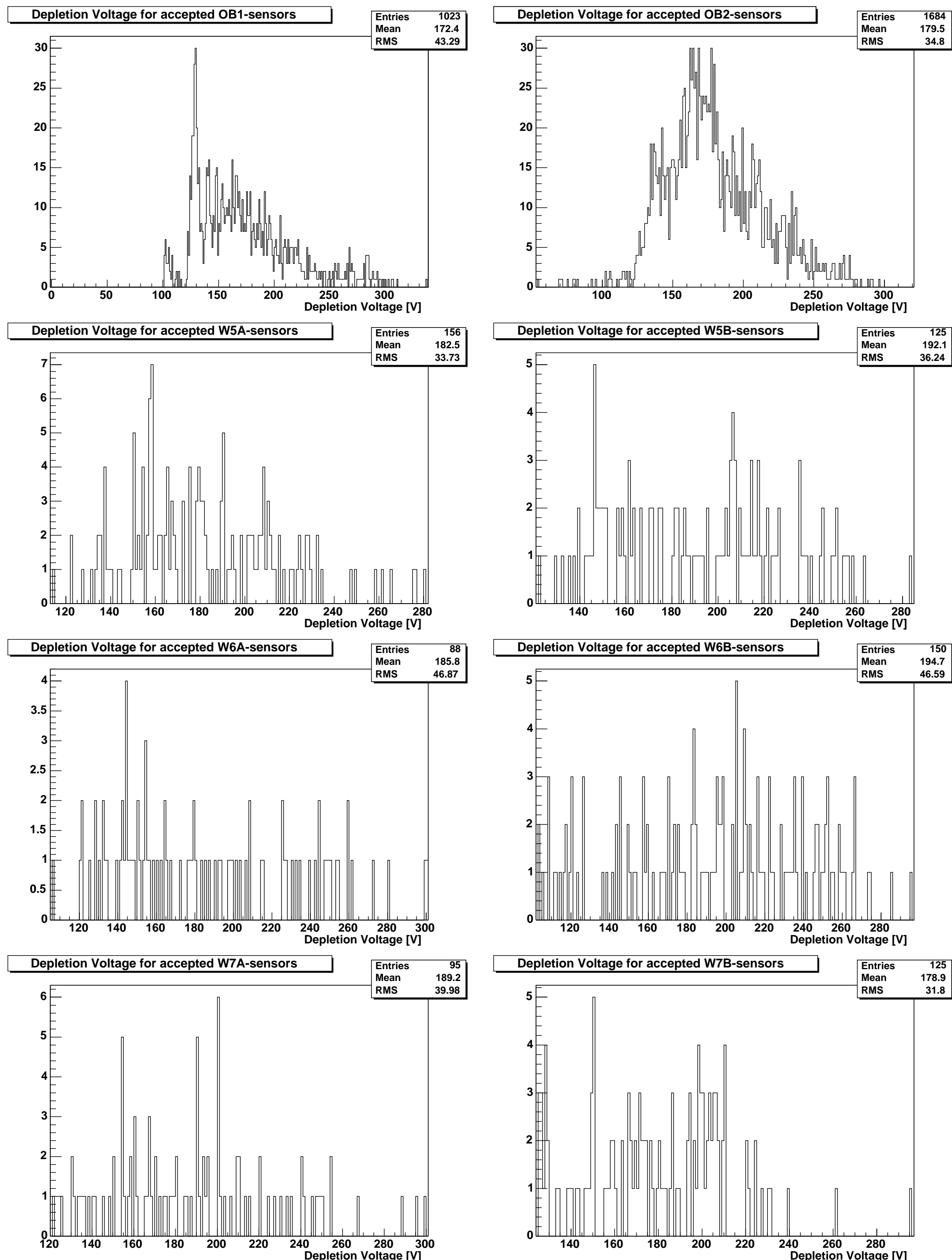

Figure 5.10: Distribution of the depletion voltages of all accepted STM sensors.

Chapter 6

Advanced Sensor Grading

6.1 Motivation

Among the first assembled modules an unexpectedly high failure rate was observerd. These modules always exhibited an extremely large noise on a few strips. The leakage currents of these strips, which caused this effect, were somtimes even so high, that the performance of the whole APV25-chip was degraded (see figure 6.3 for example). This effect is reffered to as *common mode noise* (CMN).
It is assumed, that this huge increase of the leakage current is due to defects within the bulk or at the junction, at which high electric fields lead to avalanche effects. This is referred to as *micro-discharge*. The microscopic avalanches, that should have in principle a broad high-frequency AC-spectrum, cause a well measureable increase of the macroscopic total DC-leakage current (see also section 7.2.3).
In a first attempt to solve this problem on the sensor level a new cut on the total sensor current has been proposed. In order to investigate the efficiency of such a cut a grading has been introduced. Initially two gradings were foreseen:

- Sensors with a total leakage current at 450 V below 1.5 μA, that in addition passed all other PQC- and QTC-measurements, are graded as *Grade A*.
- Sensors with a total leakage current at 450 V between 1.5 μA and 10 μA, that in addition passed all other PQC- and QTC-measurements, are graded as *Grade B*.

This cut-value of 1.5 μA, which in the beginning had been chosen based on experience, could be proved to be very sensible (see also figures 6.1 and 6.2): From the data of 1149 STM-sensors, coming from the finalised production series, the average number of single strips having a leakage current above 100 nA is drastically increased. Furthermore, only 6 out of 472 Grade A-sensors have more than 3 leaky strips, which means that the probability of having a total number of bad strips bigger than 1% of the total number of strips is rather small. Thereby the total number of bad strips also includes strips having for instance bad C_{AC}- or R_{poly}-values.
To get a better understanding of what effects lead to these problems, an advanced grading scheme has been introduced. Its goal was to distinguish between sensors

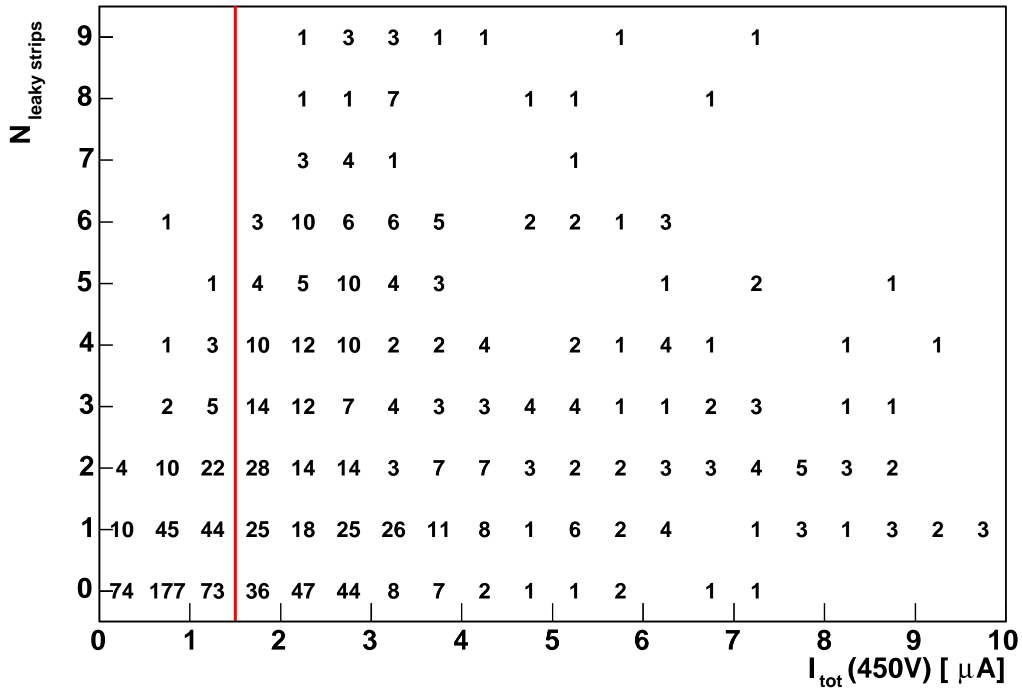

Figure 6.1: Two-dimensional histogram showing the total sensor current at 450 V (I_{tot}(450 V)) versus the number of strips with leakage currents above 100 nA ($N_{leaky\,strips}$) for 1149 STM-sensors coming from the fixed production line. For each bin the number of entries is shown as numerical value. For sensors with more than 1.5 μA sensor current the probability of having more than 1% of bad strips is drastically increased.

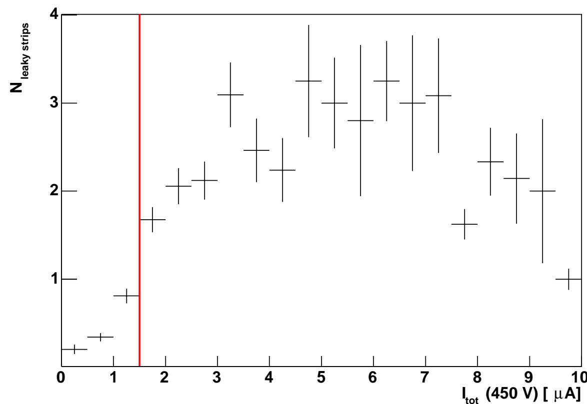

Figure 6.2: Histogram showing the average number of leaky strips ($N_{leaky\,strips}$) in dependence on the total leakage current at 450 V for 1149 STM-sensors coming from the fixed production line.

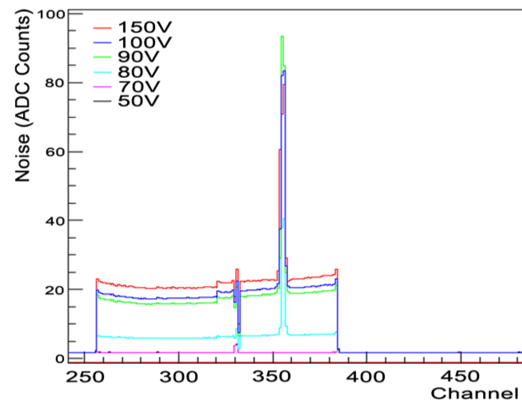

Figure 6.3: Example for a ready assembled module exhibiting extreme noise on a few strips, that degrade the performance of a whole APV25-chip.

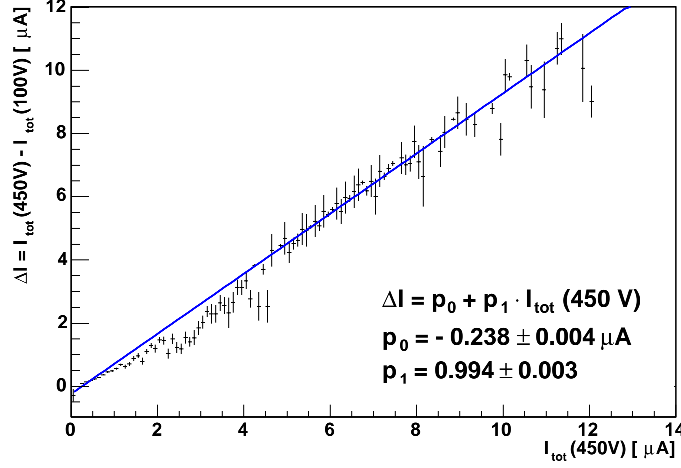

Figure 6.4: Correlation between $\mathrm{I_{tot}}(450\,\mathrm{V})$ and $\Delta\mathrm{I}$ for all STM-sensors coming from the fixed production line.

having a low or high probability to develop CMN, based on the available QTC-measurements, i.e. without being forced to introduce new measurements, like for instance AC-tests, to the QTC-procedure.

6.2 The Grading Procedure

The new grading procedure is mostly based on a more detailed scheme for sensors having less than 1.5 μA, whereas a new grading category, called *Grade A** or *Grade A+*, for sensors with perfect properties is introduced in addition to the Grade A-category. This was done mostly due to the frequent occurrence of kinks, i.e. an ohmic current increase atop of the usual sensor IV-curve. Quantitatively this can be described as the current increase between 100 V and 450 V (see figure 6.4):

$$\Delta\mathrm{I} = \mathrm{I_{tot}}(450\,\mathrm{V}) - \mathrm{I_{tot}}(100\,\mathrm{V}) \tag{6.1a}$$

$$\Delta\mathrm{I_{fit}} = p_0 + p_1 \cdot \mathrm{I_{tot}}(450\,\mathrm{V}) \tag{6.1b}$$

$$p_0 = -0.238 \pm 0.004\,\mu\mathrm{A} \quad p_1 = 0.994 \pm 0.003 \tag{6.1c}$$

Equation (6.1b) can be rewritten to:

$$\mathrm{I_{tot}}(450\,\mathrm{V}) \approx 240\,\mathrm{nA} + \Delta\mathrm{I} \tag{6.2}$$

This correlation indicates that the sensors have up to at least 100 V an usual IV-behaviour and that any anomalous effects appear at higher voltages, since ΔI is the current increase between 100 V and 450 V and the variance of the offset is very small.

Even if the effect of micro-discharge is caused by only a few strips per sensor, it was decided not to include a cut on the leakage current of single strips. This is due to the following reason: Firstly, the leakage currents of the single strips are, in

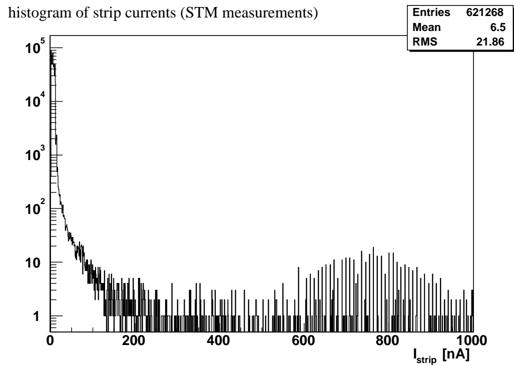

Figure 6.5: Histogram of the measured single strip currents for STM-sensors. The cut of 1 μA maximum leakage current is due to the pre-selection of sensors by the company.

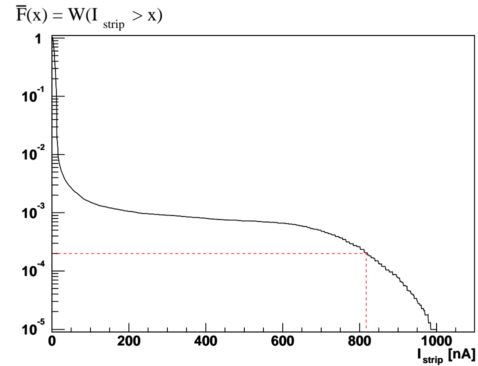

Figure 6.6: Probability distribution function for single strip currents. The marked probability of $2 \cdot 10^{-4}$ corresponds to have 1 bad strip out of 5000 strips.

contrast to the IV-curves, not measured for all sensors at the QTCs, which would make it necessary to use data from the suppliers who do this measurement for all sensors. Unfortunately effects like micro-dicharges seem to evolve with time, i.e. they normally only show up after a sensor has been ramped up and down several times, such that the company-data is not significant. Secondly, if one assumes in a worst case scenario, that 10% of all sensors have one extreme leaky strip that causes problems, i.e. approximately 1 out of 5000 strips has a current that subsequently leads to micro-discharges, one would have to introduce a cut-value of more than 800 nA (see figures 6.5 and 6.6). Such an extreme high leakage current is visible in an IV-curve anyway, such that there is no need to include the data from single strips.

Above the depletion voltage a sensor's leakage current has normally saturated, such that the IV-curve should in principle be a straight line with a very small slope. Any defect, that appears above 100 V should therefore be observable as superimposed current increase. Due to this behaviour an IV-curve can be sensible characterised by a twofold linear fit in order to get all properties for a subsequent grading (see also figure 6.7).

The IV-curves are observerd in the range from $V_{start} = \min(120\,V, V_{depl})$ and 450 V. For a given IV-curve with N entries $\{x_1, \ldots, x_N\}$ one has therefore to calculate $N-2$ fits, where the first linear fit is done in the range $\{x_1, \ldots, x_i\}$ and the second one in the range $\{x_i, \ldots, x_N\}$. The final fit is then the one with the smallest χ^2. All properties that are relevant for the subsequent grading are calculated from this final fit.

Via the χ^2 the second cut-criteria[1] for Grade A* can be defined: In order to exclude sensors that have an abnormal IV-behaviour apart from superimposed ohmic current increases, like for instance an early breakthrough, a grade A*-sensor must have $\chi^2_{\mathrm{Grade\,A^\star}} \leq 20\,\mathrm{nA}^2$. This value comes only from experience, but guarantees in general fits of the quality as shown in figure 6.7.

[1]The first cut-criteria is of course the value of $I_{tot}(450\,V)$.

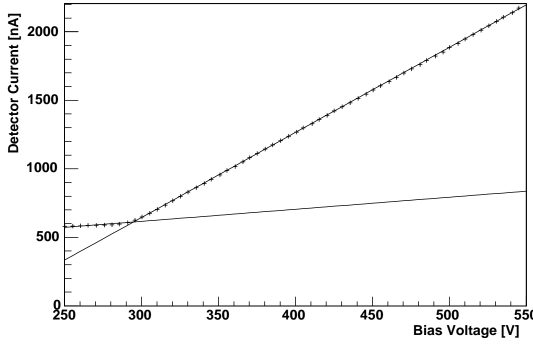

Figure 6.7: Example for a twofold linear fit for a sensor IV-curve.

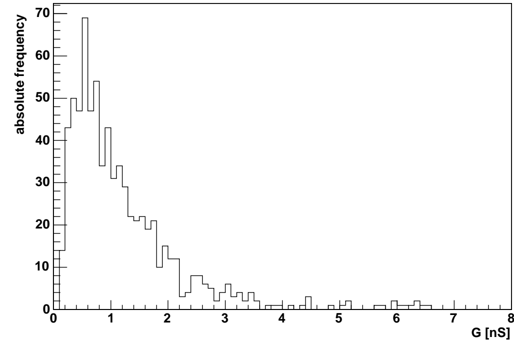

Figure 6.8: Distribution of the conductances of the kinks for OB1-sensors with ohmic current increases.

If one defines V_{kink} as the voltage at which the two straight lines of the linear fits intersect, the result can be rewritten in the form:

$$I = G \cdot (V - V_{start}) + I_{start} \qquad V_{start} \leq V \leq V_{kink} \tag{6.3a}$$

$$I = (G + \Delta G) \cdot (V - V_{kink}) + I_{kink} \qquad V_{kink} \leq V \leq 450\,V \tag{6.3b}$$

Using this form, on can define a third and a fourth cut-criteria:

- The IV-curve should not be kinked. Nevertheless even for excellent sensors ΔG does not vanish. Therefore a maximum increase of 10% w.r.t. the average conductance $\overline{G}$ of all sensors of the corresponding sensor type is requested:

$$\Delta G \leq \frac{\overline{G}}{10} \tag{6.4}$$

- The value of G itself should not be too large. A high value indicates a defect, which causes an current increase even at low voltages, such that no obvious kink in the region of $[V_{start}, 450\,V]$ can be observed. Therefore one requests:

$$G + \Delta G \leq \overline{G} + \sigma_G \tag{6.5}$$

  Thereby σ_G is the variance of the conductances G of all sensors of the corresponding type.

Figure 6.8 shows an example of the distribution of ΔG for OB1-sensors. One can easily see the peak at approximately 0.6 nS, representing sensors having no IV-kink, and a long tail towards bigger values.
Regarding the cuts on the χ^2 and the conductances, this improved grading scheme for sensors having a total leakage current below 1.5 μA can of course also be applied to sensors with currents between 1.5 μA and 10 μA, such that one gets a fourth category. This category is called *Grade B⋆*. For example, sensors with too high leakage currents due to surface currents caused by contaminations of the oxide layer during production, but perfect IV-behaviour otherwise, are typical candidates for a Grade B⋆-grading.

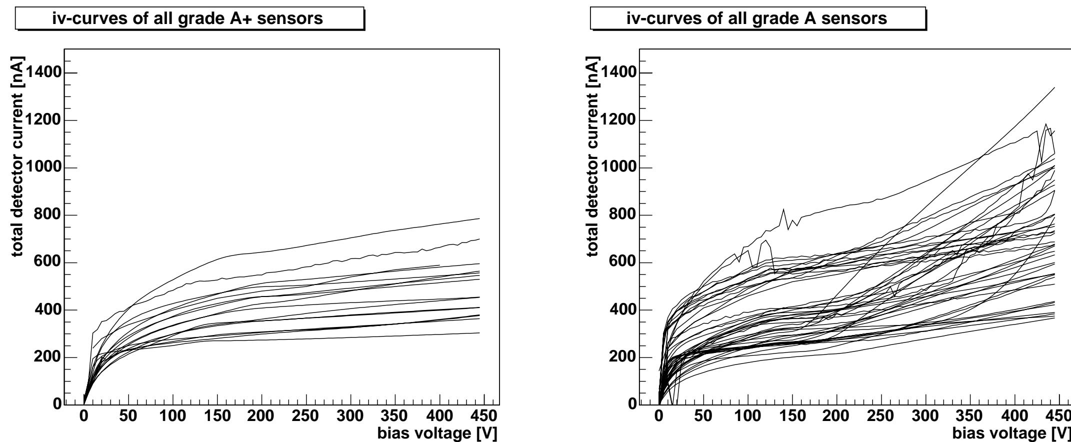

Figure 6.9: Plots produced by the sensor grading tool, showing the IV-curves of Grade A*- and Grade A-sensors of a W5B-batch.

6.3 Implementation

The grading is mostly of importance for the Gantry Centers that glue the sensors on the module frames. Unfortunately the new grading procedure is neither done by the QTCs nor implemented directly within the framework of the Tracker Database. Hence a stand-alone tool had to be developed that can be easily used by the Gantry Centers. In order to accomplish that, a program has been written using standard C++ to ensure compatibility with as much platforms as possible. As in the case of the *visualDB*-application, only the *libxml2*-library for XML-parsing and *ROOT* for the Graphical User Interface (see figure 6.10) and histograming were used in addition.

For grading a sample of sensors only a simple list containg the associated object-IDs has to be provided by the user. By selecting the list via a file-dialog and starting the grading procedure, the program extracts all needed data directly from the database and classifies the sensors according to above criteria. The graphical output contains a list of object-IDs and a plot of the IV-curves for each grading seperately (see for example figure 6.9).

In order to be more flexible, the grading tool also allows to process IV-data that comes not from the database, but is directly supplied by the user. This is for instance important if sensors are remeasured after shipping from a QTC to a Gantry Center.

By saving the data, additional information that is relevant for the Gantry Centers is added to the lists for the different gardings: For each sensor also the depletion voltage and the number of strips to leave unboned is contained in the output-files. Thereby the number of strips to leave unbonded depends on the position of strips having problems with I_{diel} or C_{AC}, and is computed as defined by the Bonding Working Group. As not all sensors are measured at the QTCs, but sometimes only random samples of a batch, the tool is able to extract company-data for supplying the needed information.

By now the grading tool is used by all Gantry Centers and is reported to work stable and flawless.

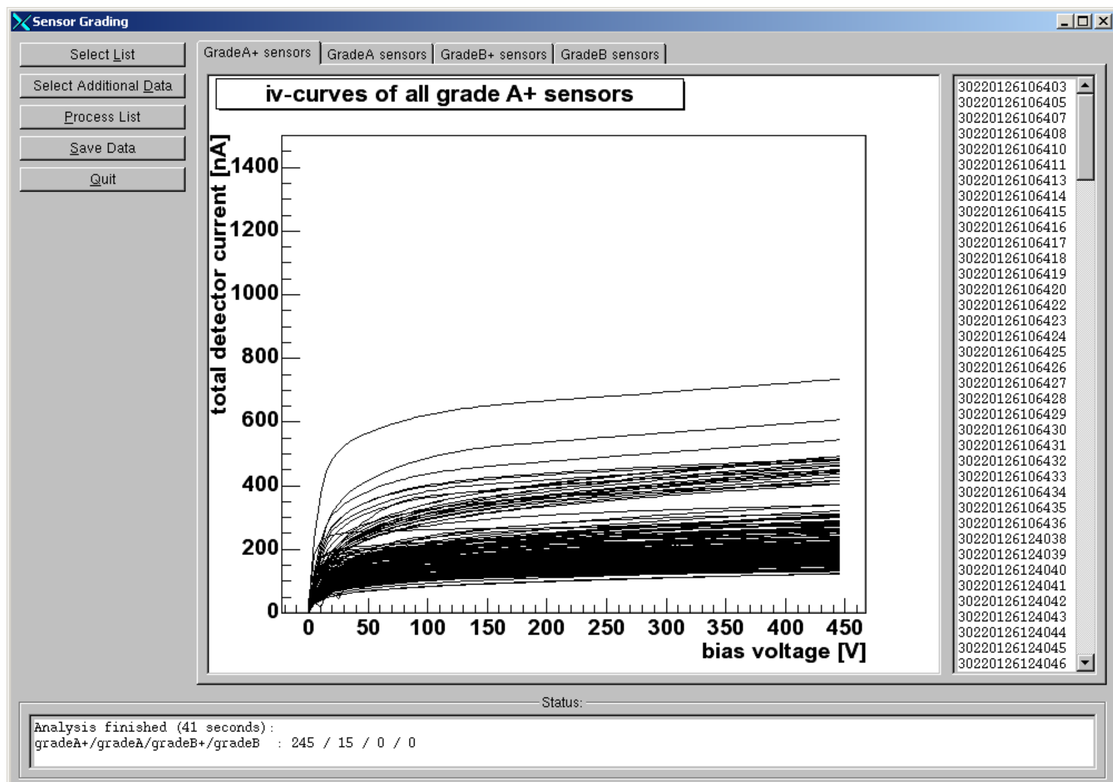

Figure 6.10: Graphical User Interface for the sensor grading tool.

6.4 Results

6.4.1 Grading Statistics

The following listing shows the gradings for the different types for accepted sensors produced up to now (according to the Tracker Database). For HPK-sensors only random samples have been measured at the QTCs, such that the corresponding values comprise not to the whole production, but just give a qualitative overview.

type	Grade A*	Grade A	Grade B*	Grade B	A/A* [%]
IB1	249	17	0	0	7
IB2	735	44	0	6	6
OB1	130	645	5	267	496
OB2	470	712	29	403	151
W1	11	1	0	0	9
W2	29	0	0	0	0
W3	87	5	0	0	6
W4	61	4	0	0	9
W5A	46	145	0	27	315
W5B	37	93	0	37	251
W6A	24	72	0	24	300
W6B	28	125	4	36	446
W7A	47	141	7	92	300
W7B	66	138	0	54	209

6.4.2 Failure Rate of Assembled Modules

To examine the efficency of the grading procedures regarding the failure rate of modules the collaboration decided to assemble TOB-modules, containing only sensors of the same grade, for testing purposes. The results are shown in table 6.1. The sensors are subdivided into three time periods, namely the pre-production (prior to week 39, 2001), the production where still improvements have been implemented (week 39, 2001 - week 12, 2003) and the finalised production series (after week 13, 2003). For each period and grading the total number of sensors, the number of sensors exhibiting extreme common mode noise and the corresponding ratio in percent is shown. As expected, modules made of Grade A*/Grade A-sensors show a better performance than those consisting of Grade B-sensors. Less expected is that there is no significant difference between Grade A* and Grade A or the year of fabrication.

sensor grade	2001/2002			2002/2003		
	quantity	CMN	%	quantity	CMN	%
Grade A*	32	1	3.1	4	1	25.0
Grade A	42	2	4.8	11	1	9.1
Grade B	22	3	13.6	10	2	20.0
total	96	6	6.2	25	4	16

sensor grade	2003			total		
	quantity	CMN	%	quantity	CMN	%
Grade A*	12	0	0.0	48	2	4.2
Grade A	16	1	6.3	69	4	5.8
Grade B	1	0	0.0	33	5	15.2
total	29	1	3.4	150	11	7.3

Table 6.1: Compilation of the sensors used for TOB-modules containing two OB2-sensors. The sensors are subdivided into three time periods: the pre-production (prior to week 39, 2001), the production where still improvements have been implemented (week 39, 2001 - week 12, 2003) and the finalised production (after week 13, 2003). The total number of sensors, the number of sensors exhibiting extreme common mode noise and the corresponding ratio in percent is shown for each period and grading.

6.5 Conclusion

Even if grading procedures do not solve problems of the sensor quality, it enables the collaboration to select sensors with the smallest failure probability. After all the failure rate could be drastically increased: Modules made of Grade B sensors show a probability of more than 15%, if only Grade A/Grade A* sensors are used the probability is less than 6%. The latter is relatively close to the goal of 4%, as demanded previous to the production by the collaboration.
The similar failure rates for Grade A and Grade A* sensors show that a real distinction between high and less qualitative sensors based on the existing QTC-measurements seems to be not possible. Nevertheless this means that it is sufficient to use a cut on the total leakage current instead of a potential current increase due to an anomalous sensor behaviour. The fact that the 1.5 μA-cut alone works that well is an indication that it is closely related with the problem itself. Thus it is also a hint for the supplier, STM in this case, and facilitates to take steps for a further improved production.

Chapter 7

Module Noise Performance

7.1 Motivation

Before the start of the massproduction of the sensors only a few prototypes of ready assembled modules existed. Until May 2004 a few hundred modules have been assembled with which the standardised tests at the Bonding Centers as well as experimental testruns with particle beams have been done.
The tests performed with these modules reach from examinations of the principal functionality to tests of the longterm-stability or the integration with the data acquisition hardware and software. This chapter focuses mainly on aspects of the noise performance of the modules, i.e. the principal noise behaviour (section 7.2) and the signal-to-noise ratio (section 7.3).

7.2 Noise Performance

7.2.1 Theory

For detectors that measure signals which correlate to an amount of absorbed energy, as in the case of silicon detectors, it is useful to quantify the noise in terms of *equivalent noise charge* (ENC). This ENC corresponds to the theoretical amount of charge that would have to be present in an ideal, noiseless detector to yield a signal as big as the actual noise of a real detector. This approach follows the same principle as for example the model of a real current generator in electronics, where the real current generator is replaced by an ideal current generator and a parallel resistor in the equivalent network.
The connection between the ENC, that can be calculated from the detector's properties, and the actual noise Σ is then given by:

$$\Sigma = \varepsilon \cdot \mathrm{ENC} \tag{7.1}$$

Thereby ε is the detectors calibration constant, i.e. the correlation between the charge produced by a traversing particle and the measured signal.
The main contribution to the noise of a detector comes from the amplifier, where the input transistor, whose noise figure depends on electrical and geometrical properties [17], is the main noise source. The contributions of further stages, such as the

integrator or the signal shaper are usually neglected, since they are in comparison rather small. Apart from the amplifier's properties, its noise depends also a lot on the load capacitance, due to its integrating nature.
In a simple approach, the amplifier noise can be described by the sum of a constant value (parallel noise) and a part that scales with the load capacitance (series noise):

$$\mathrm{ENC}_{\mathrm{amp}} = \mathrm{ENC}_{\mathrm{amp,\,parallel}} + C_{\mathrm{load}} \cdot \mathrm{ENC}_{\mathrm{amp,\,series}} \tag{7.2}$$

Apart from the amplifier, several other components contribute to the noise-figure. Figure 7.1 shows the noise related components of a typical AC-coupled strip detector configuration as used for the CMS Tracker. The AC coupling capacitor can be neglected in these considerations due to its large capacity in comparison to the load capacitance of one strip[1]. The current source I_{leak} is the fraction of the detector current seen by one strip, R_{poly} is the polysilicon resistor, C_{strip} is the load capacitance of one strip and R_{strip} is the line resistance of the implanted metal strip. In reality, the line resistance and the strip capacitance are distributed along the strip like in a transmission line, so that the effective impedance differs from the concentrated values. Nevertheless its influence is limited, such that the concentrated values can be used as a good approximation.
Leakage current fluctuations ($\mathrm{ENC}_{\mathrm{leak}}$) and the polysilicon resistor ($\mathrm{ENC}_{\mathrm{poly}}$) are parallel noise sources, while the capacitive fraction of the strip resistance noise ($\mathrm{ENC}_{\mathrm{strip}}$) is a series noise source. Numerical noise equations, in which the physical constants are already expressed by numbers, can be written as (with the peaking time T_{p}):

$$\mathrm{ENC}_{\mathrm{leak}}[\mathrm{e}] = 106 \cdot \sqrt{I_{\mathrm{leak}}[\mathrm{nA}] \cdot \mathrm{T}_{\mathrm{p}}[\mu\mathrm{s}]} \tag{7.3}$$

$$\mathrm{ENC}_{\mathrm{poly}}[\mathrm{e}] = 758 \cdot \sqrt{\frac{T_{\mathrm{p}}[\mu\mathrm{s}]}{R_{\mathrm{poly}}[\mathrm{M}\Omega]}} \tag{7.4}$$

$$\mathrm{ENC}_{\mathrm{strip}}[\mathrm{e}] = 0.395 \cdot C_{\mathrm{strip}}[\mathrm{pF}] \cdot \sqrt{\frac{R_{\mathrm{strip}}[\Omega]}{T_{\mathrm{p}}[\mu\mathrm{s}]}} \tag{7.5}$$

Parallel noise contributions rise with increasing peaking time, while series noise behaves opposite. The total noise figure is the square sum of the individual contributions, since the individual sources are uncorrelated:

$$\mathrm{ENC}^2_{\mathrm{tot}} = \sum \mathrm{ENC}^2_{\mathrm{i}} \tag{7.6}$$

The deconvolution mode (see section 3.4) comprises the noise. Both intrinsic amplifier noise components increase due to the signal processing. The external series noise is increased, while the external parallel noise terms are reduced. The ratio between peak mode and deconvolution mode noise can be expressed for parallel

[1]The load capacitance C_{strip} and the AC coupling capacitance C_{AC} are in series, such that $C^{-1}_{\mathrm{tot}} = C^{-1}_{\mathrm{strip}} + C^{-1}_{\mathrm{AC}} \approx C^{-1}_{\mathrm{strip}}$

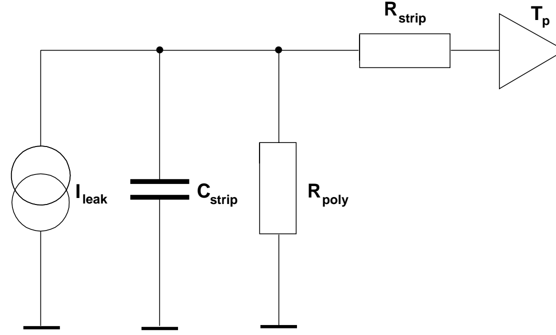

Figure 7.1: Equivalent network for a single strip and its associated readout.

and series terms as:

$$\frac{\mathrm{ENC}_{\mathrm{parallel,\,dec}}}{\mathrm{ENC}_{\mathrm{parallel}}} = \frac{e^{-2}}{x^2}\left(e^{2x} - 4x - e^{-2x}\right) \tag{7.7a}$$

$$\frac{\mathrm{ENC}_{\mathrm{series,\,dec}}}{\mathrm{ENC}_{\mathrm{series}}} = \frac{e^{-2}}{x^2}\left(e^{2x} + 4x - e^{-2x}\right) \tag{7.7b}$$

In above equation $x = T/T_{\mathrm{p}}$ is the ratio between sampling and peaking time.

7.2.2 Common Mode and Pedestal Subtraction

In an experimental setup, where apart from the module itself also the whole data acquisition hardware is present, various effects can contribute to the final signal. This means, that atop of the actual physical signal with the associated noise, as described in the previous section, additional contributions are in general superimposed. These contributions have to be taken into account when processing the raw data and as good as possible subtracted for a sensible physics analysis.

The most important effect is an offset of the signal, that comes from differences of the potentials of the various devices within the readout chain. By subtracting the average signal of all strips, that belong to one readout chip, from the signal of each individual strip, this offset can be eliminated. This procedure is called *common mode subtraction* and has to be done for each event seperately.

High leakage currents of single strips cause a permanent measureable background. Since these currents are in general constant, one has only to subtract the average common mode corrected signal, that is caused this way, for each single strip. This average common mode corrected signals are called *pedestals*, the procedure is normaly referred to as *pedestal subtraction*. For calculating the pedestals the average of several hundred events is in general sufficient.

Finaly the noise for each individual channel is defined as the variance of the common mode and pedestal subtracted signals. Its value is of most importance for identifying events, where one looks for signals being several times higher than the noise. In practice it feasible to calculate the variance of a several hundred events to get sensible values.

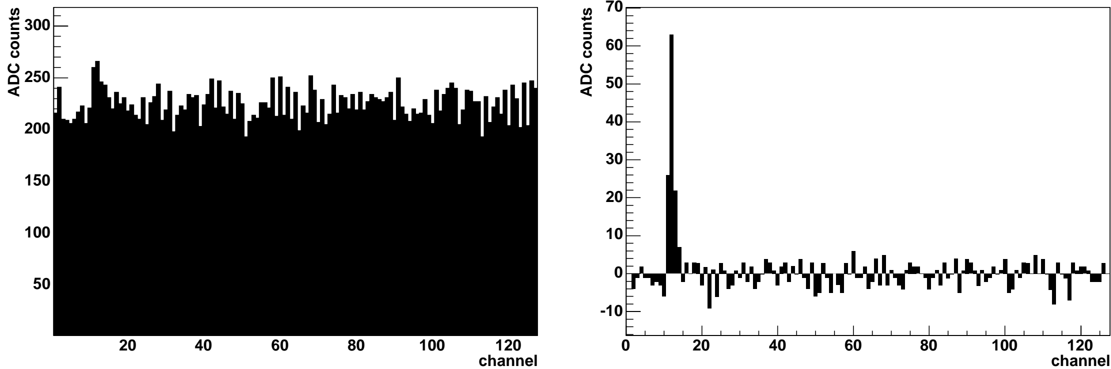

Figure 7.2: Raw (left) and final common mode and pedestal subtracted signal (right) of a simulated event.

In figure 7.2 one can see the effectivity of this procedure for a simulated event. The simulation has been done with ORCA[2], the official reconstruction framework for CMS, using standard algorithms for both the common mode and the pedestal subtraction. The pedestals were defined in advance via a random generator using an equal distribution, the common mode offset as well as the noise for each individual channel were added via a gaussian random generator for every event. Also a cluster, distributed over a few channels, has been added to each event with randomly position and height. During the simulation each the pedestals and the noise have been calibrated using 5000 events, leading to results of the quality as shown in the figure.

7.2.3 Results

Experimental Examination of the theoretical Correlation

The dependence of the total noise figure on the leakage current is of special interest. From equations (7.2-7.5), together with equations (7.1) and (7.6), one can conclude, that the total noise depends on the square root of the leakage current:

$$\mathrm{ENC}_{\mathrm{tot}}(I_{\mathrm{leak}}) = \sqrt{A^2 + B^2 \cdot I_{\mathrm{leak}}} \tag{7.8}$$

$$\Sigma\,(I_{\mathrm{leak}}) = \varepsilon \cdot \mathrm{ENC}_{\mathrm{tot}}(I_{\mathrm{leak}}) \propto \sqrt{1 + C^2 \cdot I_{\mathrm{leak}}} \tag{7.9}$$

To examine this relation the incidenting light of an one-dimesional array of LED-diodes has been used to produce an artificial leakage current within the sensor. Since it is very difficult to measure the leakage current itself on a ready assembled module, the dependence of the noise on the LED's power P_{LED} has been investigated: I_{leak} is proportional to the number of photons N that arrive at the sensor's surface. N depends linearly on the intensity of the LED-light, which in turn is proportional to P_{LED}. Therefore the correlation between Σ, or the relative noise

[2]Object-oriented Reconstruction for CMS Analysis

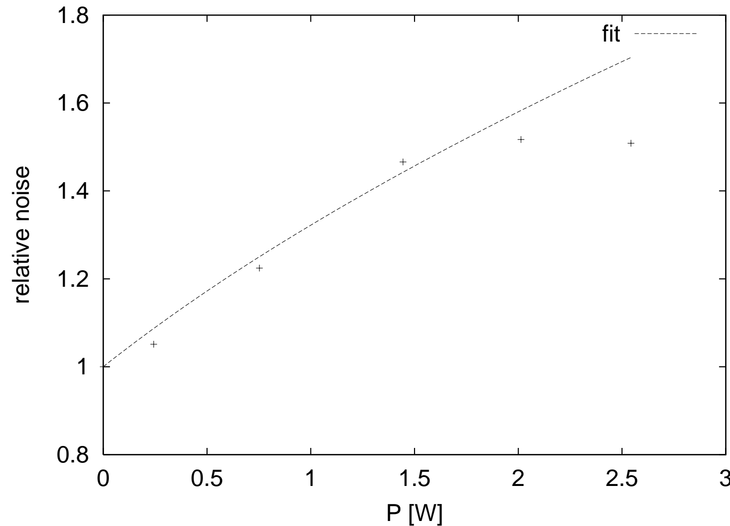

Figure 7.3: Dependence of the relative noise on the applied power.

respectively, and P_{LED} has to be of the same kind as equation (7.9) as long as no saturation effect takes place:

$$\frac{\Sigma\left(P_{\text{LED}}\right)}{\Sigma\left(P_{\text{LED}}=0\right)} = \sqrt{1 + D^2 \cdot P_{\text{LED}}} \tag{7.10}$$

The measurements have been performed using a Ring 5-module (TEC). In order to avoid spatial inhomogenities of the illumination and dependencies on other parameters, such as different intrinsic noise levels of different amplifiers, only one APV was readout. The channels coresponding to this APV were positioned perpendicular directly under the LEDs, guaranteeing a homogenious irradiation. P_{LED} was determined via a direct measurement of the array's operational voltage and the associated current. The noise of each of the 128 channels was determined from 50000 measurements using the Aachen Readout Controller System (ARCS) [18].
Figure 7.3 shows the results: The dashed line represents a fit through the first four measuring point. Therefore it is only a guide for the eye, but it indicates that the predicted correlation in equation (7.10) is covered. Furthermore the expected saturation due to the fact, that the incidenting photons produce electron-hole pairs only near the surface, can be seen.

Results from assembled TOB-modules

For the first assembled TOB-modules, the noise performance in dependence on the currents of single strips has been of great interest. The theoretical correlation predicts a noise increase of at most 20 percent for strips with leakage currents as high as 1 μA in comparison to strips with almost no leakage current. This would mean that an extreme increase of the noise level due to single strips (as for the module in figure 6.3) can not be explained by standard noise theories but for instance by micro-discharge effects.
The TOB-modules used here consist of two electrically daisy-chained OB2-sensors,

such that the strip resitances R_{strip} of two daisy-chained strips are in series while the associated capacitances C_{strip} and the polysilicon resistors R_{poly} are parallel. The strip resistance R_{strip} can be calculated via the resistivity of the implant, which is measued at the PQCs, while the resistance R_{poly} is measured for each strip by the QTCs. Therefore this data is available via the Tracker Database. The capacitance C_{strip} is not measured so that it has to be calculated via an empirical formula [10]:

$$C_{\text{strip}} = C_{\text{int}} + C_{\text{back}} = 0.8 + 1.6 \cdot \frac{w_{\text{strip}}}{p_{\text{strip}}} \, [\text{pFcm}^{-1}] \tag{7.11}$$

The capacitance per unit length does only depend on the ratio of strip width w_{strip} to strip pitch p_{strip}, which is for all CMS silicon sensors a fixed value, and not on the sensor's thickness. This comes from the fact, that the capacitance between a strip and the backplane C_{back} increases with increasing thickness while the interstrip capacitance C_{int}, which is parallel to C_{back}, decreases with increasing thickness, such that C_{strip}, which is simply the sum, stays approximately constant.
The experimental data comes from the module tests after the assembly in the Gantry Centers at Fermilab[3] and UCSB[4]. The data was taken using ARCS, which processes the raw data from the modules the same way as it will be done in the final experiment, such that the results are significant for the modules' noise performance in the finished Tracker. This also includes common mode and pedestal subtraction. To compare these experimental results with the theoretical prediction, the *relative noise* has been investigated:

$$\frac{\Sigma\,(I_{\text{leak}})}{\Sigma\,(I_{\text{leak}}=0)} = \frac{\text{ENC}\,(I_{\text{leak}})}{\text{ENC}\,(I_{\text{leak}}=0)} = \sqrt{1 + \alpha \cdot I_{\text{leak}}} \tag{7.12}$$

The left side of equation (7.12) represents the data from 57 modules, showing no obvious defects, where $\Sigma\,(I_{\text{leak}}=0)$ is taken as the noise of daisy-chained strips where the sum of both leakage currents is less than 4 nA, which leads to a maximum (theoretical) error of 4 ‰. Strips, that have according to the Tracker Database an I_{leak}-entry bigger than the total detector current at 450 V, are excluded, since these entries are believed to be measuring errors. For example at the QTC in Perugia a bad contact can result in an extremely high value due to the setup. Also unbonded strips as well as the first and last two strips of each APV25-chip, which are known to have a slightly higher noise, are not included. This results in a total number of 28167 investigated strips.
The right side of equation (7.12) is the theoretical relative noise according to section 7.2.1, using the average values of R_{strip}, R_{poly} and C_{strip}. For the APV25-chip the noise figures for both modes are:

$$\text{ENC}_{\text{APV}}\,[\text{e}] = \begin{cases} 250 + 36\text{pF}^{-1} & \text{peak} \\ 400 + 60\text{pF}^{-1} & \text{deconvolution} \end{cases} \tag{7.13}$$

The results are shown on the pages 73 and 74. High leakage currents are very rare, such that for the direct examination only the noise of strips with at most 60 nA

[3]Fermi National Accelerator Laboratory, Batavia, IL, USA
[4]University of California, Santa Barbara, CA, USA

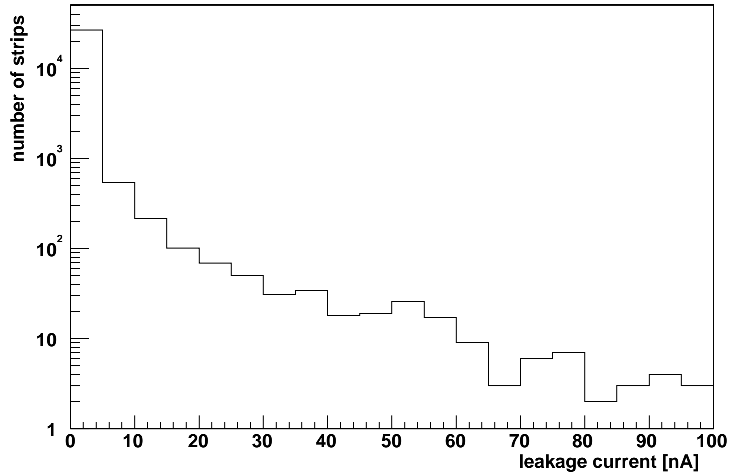

Figure 7.4: Absolute frequency of the measured leakage currents.

leakage current have been taken into account. This guarantees, when using a bin width of 5 nA, to have more than ten entries per bin and therefore a reasonable statistics for fitting the data (see figure 7.4).
For small currents the theoretical correlation and the average measured signal agree very good. Figures 7.8 and 7.10 show the average relative noise level together with the corresponding variance in dependence on the leakage current for currents up to 60 nA. For deconvolution mode, where the observed effect is only in the percentage level, α_{fit} and α_{theory} are very close together, while in peak mode the difference is slightly bigger. Since for peak mode the predicted relative noise is bigger than the actual measured average relative noise, this indicates that the underlying noise $\text{ENC}_{\text{tot}}\,(I_{\text{leak}} = 0)$ is slightly larger than expected. Nevertheless the theoretical predictions agree very good with the experimental results.
Figures 7.7 and 7.9 show the relative noise in dependence on the measured leakage current for peak and deconvolution mode for all investigated strips. Two things are remarkable when looking not only on small currents and the average relative noise: Firstly, even for large leakage currents the experimental results are mostly close to the predictions or smaller, indicating again a larger underlying noise level than expected. Secondly, strips that exhibit an unusual high noise, are present over the whole range of leakage currents. Thus it is very unlikely, that the presence of high leakage currents alone is responsible for extreme noise increases.

Implications on the common mode noise

As shown in the previous section, the influence of the leakage current, that arises from statistical effects within the semiconducting bulk, on the common mode and pedestal subtracted noise follows in general the theoretical prediction. This rules out, that the drastic increase of the common mode noise on some modules, where always a few strips have leakage currents of a few μA, is caused by usual noise sources, but other physical effects.
The most plausible explanation is offered by the theory of micro-discharges: Rela-

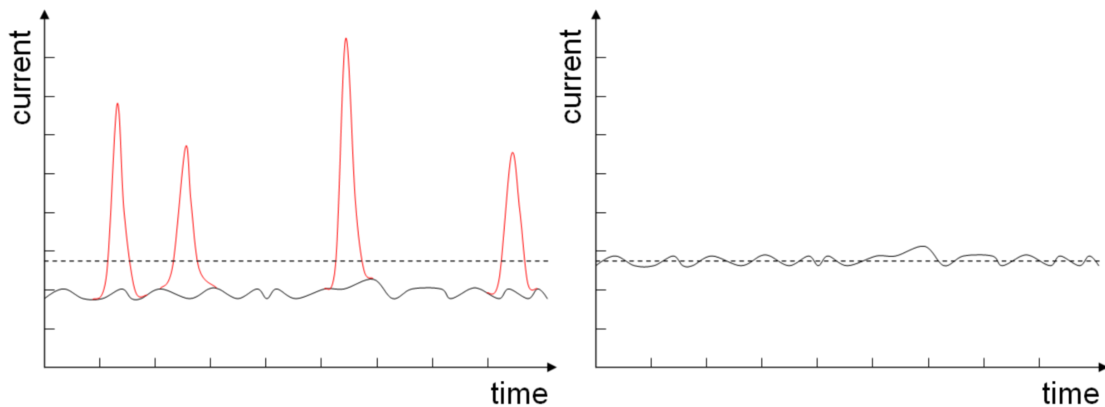

Figure 7.5: Sketch of the signal from the usual leakage current and superimposed micro-discharges (shown in red) compared to the signal of a slightly increased but otherwise usual leakage current. Integrated over time both signals have the same height, nevertheless the left signal has a huge variance, which corresponds to a high noise level.

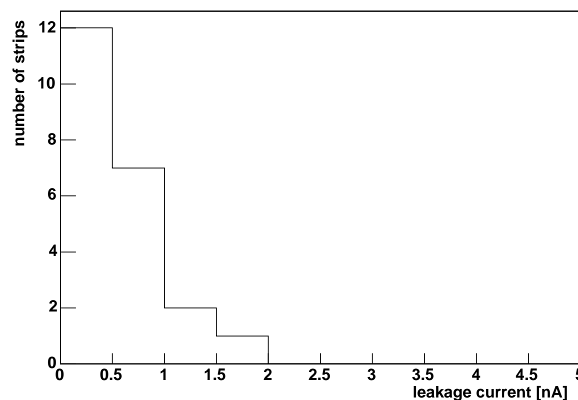

Figure 7.6: Leakage currents of the strips, that caused a large common mode noise on modules assembled before october 2003, prior to assembly (QTC-data).

tively large defects within the bulk can cause large electric fields, where avalanche effects can happen. Thus on the more or less constant usual leakage current an abnormal high-frequent signal is superimosed. If the average frequency of the micro-discharges is high in comparison to the (inverse) integration time of an ampere meter one would only measure an increased DC-current, whereas the APV25-chip, with its 40 MHz sampling frequency, would measure a very noisy AC-signal (compare to figure 7.5). The peaks of the micro-discharges could then even be so large, that the whole readout-chip would be saturated, which would of course influence the noise level of all channels, as seen on some modules. Furthermore it is consitent with the fact, that all strips, that caused the extreme common mode noise on modules assembled prior to october 2003, behaved perfectly during the QTC-measurements (see figure 7.6) since at that time the sensors had hardly been stressed, such that the defect had not appeared then.

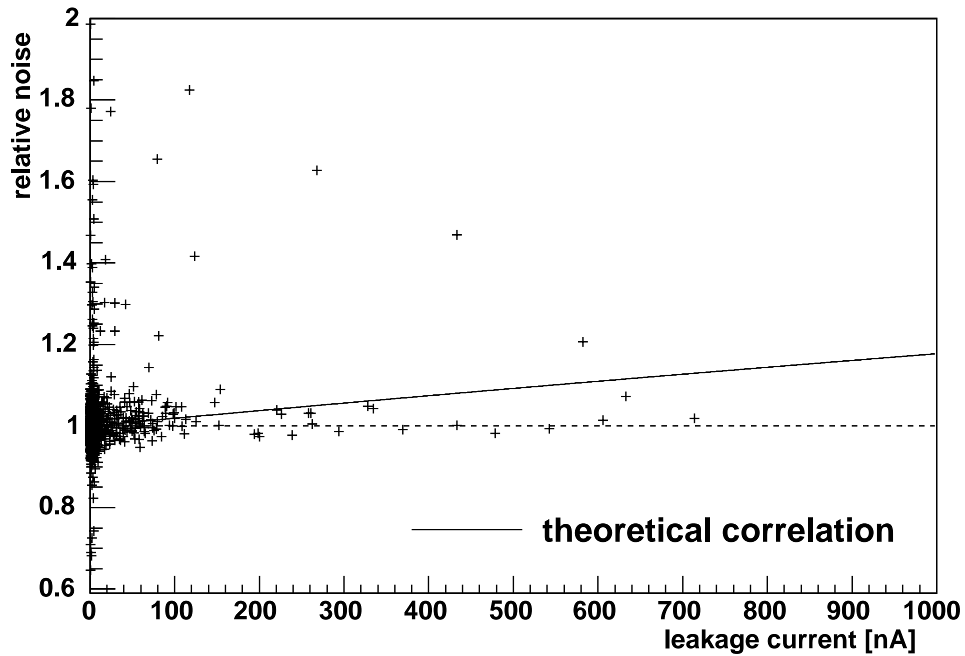

Figure 7.7: Two-dimensional histogram of the relative noise versus the leakage current in peak mode. The solid line shows the predicted correlation.

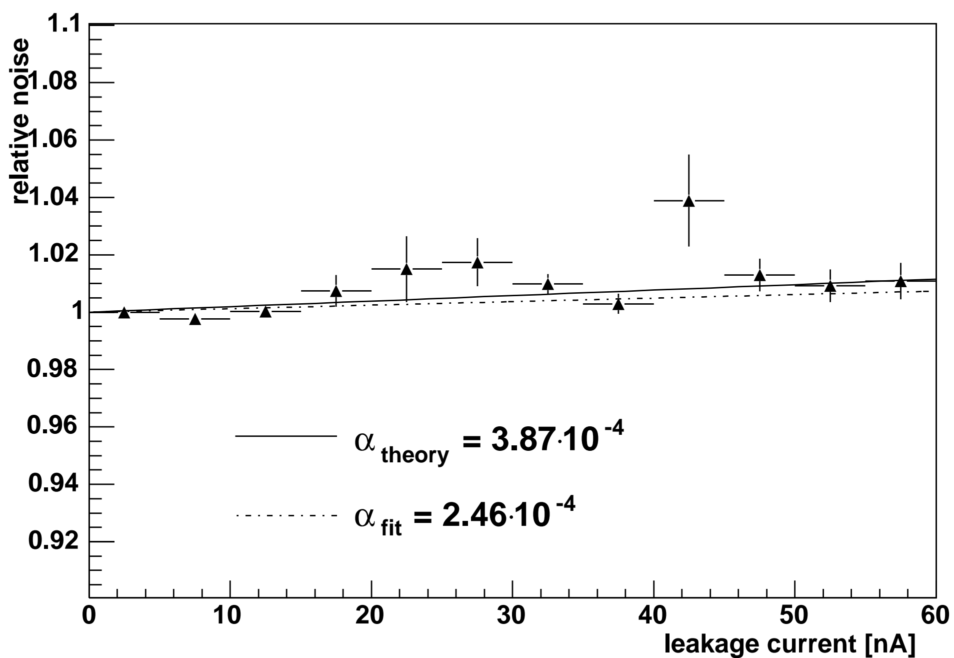

Figure 7.8: Profile histogram of the relative noise versus the leakage current in peak mode.

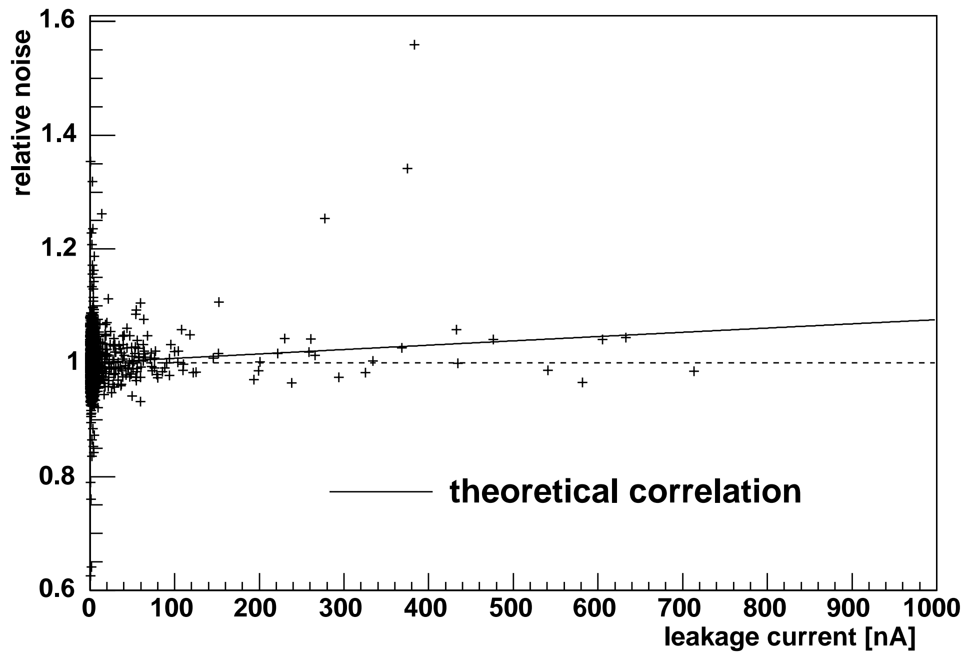

Figure 7.9: Two-dimensional histogram of the relative noise versus the leakage current in deconvolution mode. The solid line shows the predicted correlation.

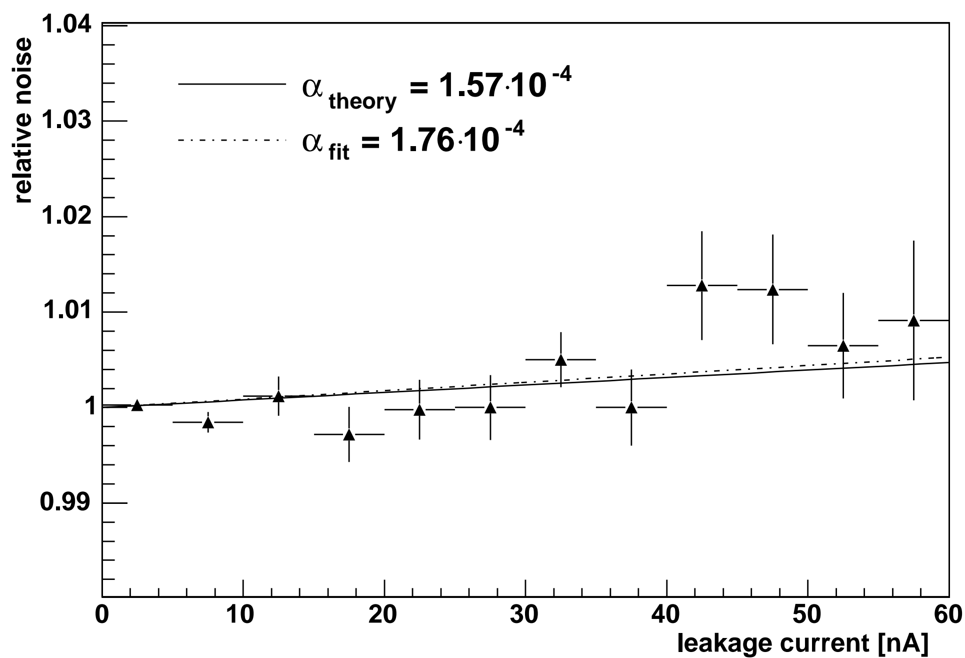

Figure 7.10: Profile histogram of the relative noise versus the leakage current in deconvolution mode.

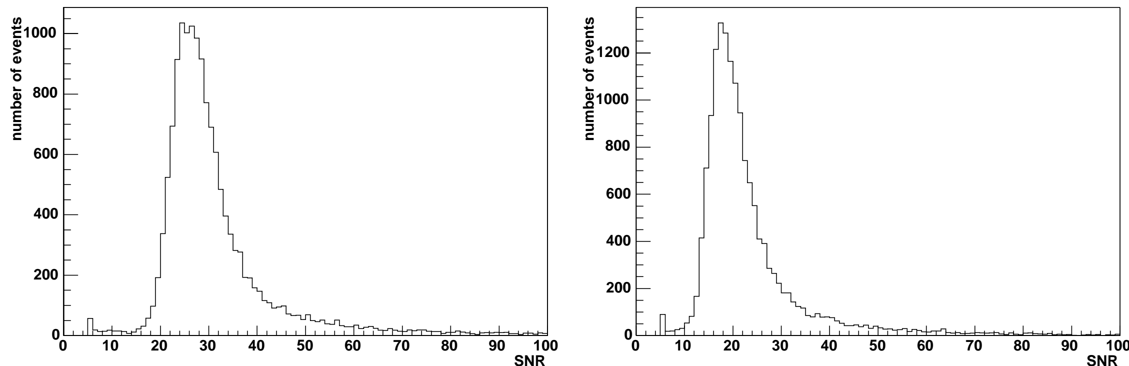

Figure 7.11: SNR figures for peak (left) and deconvolution mode (right) at 350 V for the TIB-modules used at the May 2003 testbeam at CERN.

7.3 Signal-to-Noise Ratio

For particle tracking the procedure of reconstructing tracks from the signals within the tracker is the first step. Therefore it is necessary to have a good signal-to-noise ratio in order to ensure a good pattern recognition. During May 2003 several assembled TIB-, TOB- and TEC-modules, together with support structures and a data acquisition system very close to the one that will be used in the final experiment, have been operated at the TkX5b-beamline at CERN. For runs in peak mode a beam of long bunches of 120 GeV muons, i.e. minimum ionising muons, has been used. For runs in deconvolution mode these bunches were subdivided by using RF-cavities, such that a bunch-crossing frequency of 25 ns could be simulated. For synchronising the data acquisition to this 40 MHz frequency an external trigger, consisting of scintillation detectors, has been used.
The recorded events, stored at CASTOR[5], the dedicated storage manager for the extreme data flow at LHC, have been analysed with the object-oriented reconstruction framework used for the CMS-experiment (ORCA). For the noise as well as the pedestal calibration 500 events have been used. For the cluster finder, a signal-to-noise ratio of 5 has been chosen as cut value for the cluster-seed, i.e. the signal of a channel that might be part of a cluster. From the results one can see that this is sufficient to suppress most of the background (see figure 7.11).
For the TIB-modules, consisting of one IB2-sensor each, the signal-to-noise ratio in dependence on the operation voltage is shown below for peak and deconvolution mode (figure 7.12). Thereby the signal-to-noise ratio is defined as the most probable ratio, computed via fitting the experimental data with a Landau distribution. As expected, the signal-to-noise ratios are adequate, i.e. above 15, in the foreseen HV-region of about 300 V, even for deconvolution mode.

[5]**C**ERN **A**dvanced **STOR**age Manager

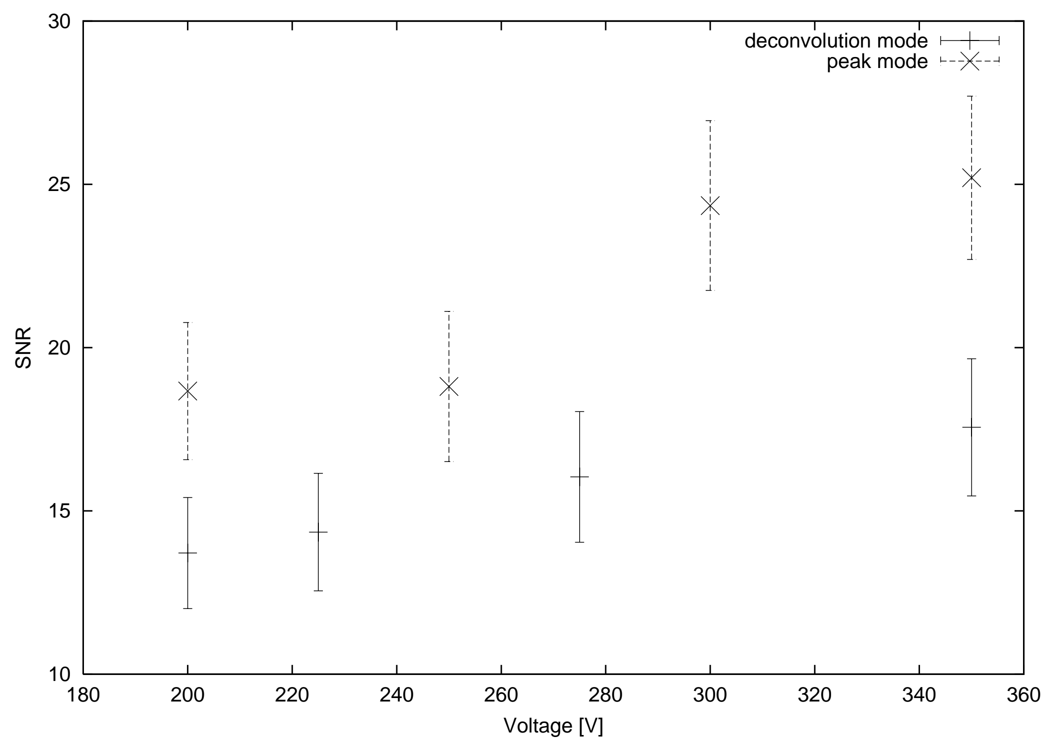

Figure 7.12: Most probable signal-to-noise ratio in peak and deconvolution mode in dependence on the HV for the TIB-modules used at the May 2003 testbeam at CERN.

Chapter 8

Conclusions

Various investigations concerning single silicon microstrip sensors as well as ready assembled modules for the CMS Tracker have been done. For the sensors emphasis has been laid on their IV-properties. In particular it could be shown that a 1.5 μA-cut on the leakage currents, that was introduced on the basis of experience, is not only sensible for classifying the sensors but also guarantees in general to have not more than 1% bad strips. Therefore a further classification for selecting the best sensors needs to look only for anomalous properties. For this reason it was decided to examine the IV-curve especially for kinks, since it is measured for most sensors with relatively little effort and is in addition accessible via the database. This new scheme introduced to the previously proposed grading categories, namely Grade A and Grade B, the additional category Grade A*. To enable the collaboration to use the corresponding grading procedures an easy to use tool has been devolped which is currently in use at the Gantry Centers.

The need to gain a deeper understanding of the dependence of a sensor's depletion voltage on the bulk's resistivity lead to a new approach to describe depleted structures such as microstrip sensors and diodes. In addition to using a simple but quite realistic and analytically solvable models for both sensors and diodes, also the inhomogenious doping concentration in real wafers was taken into account. In spite of disturbing uncertainties regarding important parameters, such as the bulk resistivity, the theoretical correlation is in remarkable agreement with the experimental results.

For modules emphasis has been laid on the topic of extreme common mode noise. The theoretical influence of the leakage current on the noise could be veryfied for the modules assembled so far. Thus it could be outruled that this problem is caused by the existence of strips with increased leakage currents alone, since usual currents of that strength would not lead to such a huge effect. The most probable explanation are micro-discharges within defects in the bulk, that lead to a high frequent and thus very noisy AC-current. Even if the newly introduced selection criteria for sensors, based on the advanced grading scheme, do not solve the problem of common mode noise completely, a clear reduction of the failure rate could be accomplished. The percentage of bad modules, assembled with Grade A/Grade A* sensors, is below 6%, which is already close to the demanded goal of 4%. Modules containing only Grade B sensors have in contrast a failure rate of 15%. To achieve

the desired quality, i.e. a loss of less than 4%, new methods and measurements, which can easily be introduced into the QTC-scheme, will be needed.
In order to make the testing centers' data and logistics information available for all people involved with the CMS Tracker Collaboration, it was decided to maintain a database. To enable the users to extract directly physics data in an appropriate manner from this database, for example PQC- or QTC-data, different tools have been developed. In this context also the visualDB-application has been developed, which is a highly flexible tool for histograming and processing various kinds of data. Especially for monitoring the quality of the produced sensors, where the observed parameters depend on the actual problem, this flexibility is of great importance.

Bibliography

[1] C.E.Wulz (CMS Collaboration), *CMS – Concept and Physics Potential*, CMS CR-1999/012, 1999

[2] CMS Collaboration, *The Magnet Project Technical Design Report*, CERN/LHCC 97-10, CMS TDR 1, 1997

[3] CMS Collaboration, *The Hadron Calorimeter Project Technical Design Report*, CERN/LHCC 97-31, CMS TDR 2, 1997

[4] CMS Collaboration, *CMS MUON Technical Design Report*, CERN/LHCC 97-32, CMS TDR 3, 1997

[5] CMS Collaboration, *CMS ECAL Technical Design Report*, CERN/LHCC 97-33, CMS TDR 4, 1997

[6] CMS Collaboration, *The Tracker Project Technical Design Report*, CERN/LHCC 98-6, CMS TDR 5, 1998

[7] Particle Data Group, *Particle physics Booklet*, Springer, 2000

[8] M.Winkler, *dE/dx in Halbleiterdetektoren*, Diploma Thesis, Vienna University of Technology, 1998

[9] Rose Collaboration (RD48), *Third RD48 Status Report*, CERN/LHCC 2000-009, 1999

[10] S.Braibant et al., *Investigation of design parameters for radiation hard silicon microstrip detectors*, Nuclear Instruments and Methods in Physics Research A 485 (2002), 343-361

[11] R.Turchetta et al., *Design and results from the APV25, a Deep Submicron CMOS Front-End Chip for the CMS TRacker*, 4$^{\text{th}}$ International Symposium on Development and Application of Semiconductor Tracking Detectors, Hiroshima, Japan, 2000

[12] S.Gadomski et al., *The Deconvolution Method of Fast Pulse Shaping at Hadron Colliders*, Nuclear Instruments and Methods in Physics Research A 320 (1992), 217-227

[13] N.Bingefors et al., *A novel technique for fast pulse-shaping using a slow amplifier at LHC*, Nuclear Instruments and Methods in Physics Research A 326 (1993), 112-119

[14] J.-L. Agram et al., *The Silicon Sensors for the Compact Muon Solenoid Tracker – Design and Qualification Procedure*, CMS NOTE 2003/015

[15] J.Rahn, *Depletion Characteristics of Silicon Microstrip Detectors*, Santa Cruz Institute for Particle Physics, SCIPP 93/12, 1993

[16] E.Barberis et al., *Capacitances in silicon microstrip detectors*, Nuclear Instruments and Methods in Physics Research A 342 (1994), 90-95

[17] E. Nygård et al., *CMOS Low Noise Amplifier for Microstrip Readout: Design and Results*, Nuclear Instruments and Methods in Physics Research A 301 (1991), 506-516

[18] M. Axer et al., *Tests of Silicon Detector Modules for the Tracker End Cap with the ARC System*, CMS NOTE 2003/002